1949

Light-induced non-adiabatic properties in molecular systems

Thesis for the Degree of Doctor of Philosophy (PhD)

Otabek Umarov

Supervisor: Prof. Dr. Ágnes Vibók

UNIVERSITY OF DEBRECEN
Doctoral Council of Natural Sciences and Information Technology
Doctoral School of Physics

Debrecen, 2024.

Hereby I declare that I prepared this thesis within the Doctoral Council of Natural Sciences and Information Technology, Doctoral School of Physics, University of Debrecen in order to obtain a PhD Degree in Natural Sciences at Debrecen University.
The results published in the thesis are not reported in any other PhD theses.

Debrecen, 2024..... Otabek Umarov
Candidate

Hereby I confirm that Otabek Umarov candidate conducted his studies with my supervision within the Atomic and Molecular Physics Doctoral Program of the Doctoral School of Physics between 2020 and 2024. The independent studies and research work of the candidate significantly contributed to the results published in the thesis.
I also declare that the results published in the thesis are not reported in any other theses.
I support the acceptance of the thesis.

Debrecen, 2024..... Dr. Ágnes Vibók
Supervisor

Light-induced non-adiabatic properties in molecular systems

Dissertation submitted in partial fulfilment of the requirements for the doctoral (PhD) degree in physics

Written by Otabek Umarov certified physicist

Prepared in the framework of the Doctoral School of Physics of the University of Debrecen

Atomic and Molecular Physics program

Dissertation advisor: Dr. Ágnes Vibók

The official opponents of the dissertation:

Dr. ....
Dr. ....

The evaluation committee:

Chairperson: Dr. ....
Members: Dr. ....
Dr. ....
Dr. ....
Dr. ....
Dr. ....

The date of the dissertation defense: .....

Contents

The glossary list

AC avoided crossing

ADT adiabatic-to-diabatic transformation

aug-cc-pV5Z augmented correlation-consistent quintuple zeta

BOA Born-Oppenheimer approximation

CAP complex absorbing potential

CI conical intersection

DOF degree of freedom

DVR discrete variable representation

EM electromagnetic

FC Franck-Condon

FFT fast fourier transformation

GP geometric phase

HF Hartree-Fock

KER kinetic energy release spectra

LIAC light-induced avoided crossing

LICI light-induced conical intersection

MCTDH multi-configuration time-dependent Hartree

MRCI multi-reference configuration interaction

NACT non-adiabatic coupling term

PDM permanent dipole moment

PES potential energy surface

SPF single-particle function

TD time-dependent

TDH time-dependent Hartree

TDM transition dipole moment

TDSE time-dependent Schrödinger equation

TI time-independent

TISE time-independent Schrödinger equation

VP variational principle

WF wave function

Introduction

During my PhD program, I studied light-induced non-adiabatic features in diatomic and polyatomic systems through the use of theoretical simulations. In this Thesis, I will detail what I have researched during my study period from 2020 to 2024.

The Born-Oppenheimer approximation (BOA) [1, 2] is the most commonly used approach in atomic and molecular physics. In this approach, the heavy nucleus moves much slower compared to the light electrons; therefore, the electron and nuclear motions can be treated separately. This approximation usually works well and provides reasonable results in molecular dynamical processes. However, the BOA becomes invalid at specific nuclear configurations, particularly near degeneracy points between potential energy surfaces of molecules [3–6]. Such cases are called non-adiabatic processes, in which strong and non-negligible non-adiabatic coupling terms (NACTs) [4, 7, 8] couple the various electronic energy states in molecules. The non-adiabatic effects [7, 9–18] can play an essential role in molecular physics and photochemistry, especially in molecular fragmentation, proton transfer or isomerization processes. The non-adiabatic effects result in significant changes in molecular spectroscopy, dissociation, geometric features, proton transfer, and so forth...[3, 19–21].

In non-adiabatic processes, the potential energy surfaces of molecular systems might intersect, and this type of intersection is known as a conical intersection (CI) [19, 20, 22, 23]. It is a usual phenomenon that CIs (or degeneracy of states) can exist abundantly in polyatomic molecules because

of the existence of many degrees of freedom. This type of CI occurring in nature is called natural CI.

It is well known that a molecular system has to hold at least two independent nuclear degrees of freedom in order to form a CI. Because there is only one vibrational degree of freedom (DOF) in diatomic molecules in field-free space, CIs can never be built up; only avoided crossings (ACs) (approaching of states each other) can emerge [9, 19]. However, when an external (classical or quantum light) field is applied to molecular systems, light-induced avoided crossings (LIACs) or light-induced conical intersections (LICIs) [11, 12, 20, 24–27] can appear, even in diatomics. By inserting an external field into the molecular system, light-matter interaction between an applied field and the molecular system appears [28, 29]. Due to this interplay, molecular dynamics such as light-induced dissociation and spectroscopic and geometric features of molecules can be studied in detail [8, 15, 16, 19, 21, 30–34]. The inserted external field can provide a rotational motion (or rotational DOF) by rotating the molecular system around the polarization direction of the external field. Unlike the natural CIs and ACs, the energy position of the LICIs and LIAC and their non-adiabatic strengths can be governed by external field parameters (like frequency and intensity in classical light). As a result, altering the parameters of an external field might control the non-adiabatic dynamics in molecules.

To explore the system's nuclear dynamics, one first needs to solve the time-independent (TI) problem by properly explaining the molecular electronic structure. The data obtained from the TI solutions can be the potential energy surfaces and dipole moments of a molecular system [35, 36]. As a next step, the time-dependent (TD) problem is solved by using the TI data so as to investigate the molecular dynamics.

In the present Thesis, I studied the light-induced non-adiabatic nuclear dynamics in molecular systems by performing computational calculations. For the diatomic NaH molecule, photodissociation dynamics are studied along with the fragment kinetic energy release spectra (KER) as well as the

fragment angular distributions of individual electronic states in the pump-probe scheme. I studied the impact of LICIs and LIAC on light-induced dissociation dynamics and the effect of this system's permanent dipole moment (PDM) on dissociation yields. The results are compared with and without the PDMs by solving both one-dimensional and two-dimensional time-dependent Schrödinger equations for nuclear motion. Furthermore, I investigated the topological properties of polyatomic formaldehyde H_2CO molecule in the presence of LICI created by a cavity quantum light. I did some research in exploring the Berry phase (or geometric phase) as well as the NACTs between two polaritonic states of this system in the vicinity of the light-induced conical intersection.

This Thesis is structured as follows: chapter 1 briefly explains the theoretical background of non-adiabatic processes, quantum chemistry calculations, light-matter interactions and molecular nuclear dynamics. Chapter 2 is devoted to studying light-induced photodissociation dynamics of NaH with the help of the pump-probe model. This chapter initially reports the electronic structure calculations and the pump and probe pulses' descriptions. In the later sections, dissociation dynamics, along with the fragment KER and angular distributions, are given in detail. Chapter 3 details the investigations of the topological properties of the formaldehyde molecule in the presence of LICI created by an optical cavity. Moreover, a short conclusion will be given at the end of each discussion chapter. The summary of the attained results will be presented in chapter 4.

Chapter 1

Theoretical background

This chapter gives detailed explanations of the theoretical background of topics related to my investigation areas, from molecular electronic structure calculations to nuclear dynamical processes. These topics help to understand the physical-chemical phenomena in the theoretical treatments of molecular systems. My research study can be partitioned into two various parts. The first part involves working with molecular electronic structures by finding potential energy surfaces (PESs), permanent and transition dipole moments (PDMs and TDMs). Usually, these data can be obtained from one of the efficient quantum packages, Molpro [35, 36]. In the second part, molecular dynamics can be calculated by using the data obtained in the first part. The nuclear dynamics can be investigated employing the multi-configuration time-dependent Hartree (MCTDH) [37–40] method, which is very accurate.

This chapter explains the theoretical background of topics involving the two parts mentioned above. At the beginning of this chapter, fundamental concepts of the BOA for many-electron molecular systems will be given. After that, the fundamental theory of molecular electronic structure calculations and the method used are discussed. The adiabatic and diabatic representations, as well as the CIs, will be detailed in the next sections. Subsequently, the fundamental theories of the interaction of molecular sys-

tems with classical and quantized external fields are discussed. At the end of this chapter, molecular nuclear dynamics are reported in detail.

1.1 The Born-Oppenheimer approximation

If we consider the polyatomic molecule having n_e electrons, N nuclei, and the corresponding masses m_e and M_α of these particles, respectively, the system's total TI Hamiltonian can include the kinetic energy operators of electrons ($\hat{T}_e$) and nuclei ($\hat{T}_N$), electron-electron potential energy (V_{ee}), nuclear-nuclear potential energy (V_{NN}), and electron-nuclear potential energy (V_{eN}):

$$\begin{aligned}\hat{H} &= \hat{T}_N(\vec{R}) + \hat{H}_e(\vec{r},\vec{R}) = \hat{T}_N(\vec{R}) + \hat{T}_e(\vec{r}) + V_{ee}(\vec{r}) + V_{NN}(\vec{R}) + V_{eN}(\vec{r},\vec{R}) \\ &= -\sum_{\alpha=1}^{N}\frac{\hbar^2}{2M_\alpha}\nabla^2_{R_\alpha} - \sum_{i=1}^{n_e}\frac{\hbar^2}{2m_e}\nabla^2_{r_i} + \sum_{i=1}^{n_e}\sum_{\substack{j=1\\j>i}}^{n_e}\frac{1}{4\pi\varepsilon_0}\frac{e^2}{|\vec{r_i}-\vec{r_j}|} \\ &\quad + \sum_{\alpha=1}^{N}\sum_{\substack{\beta=1\\\beta>\alpha}}^{N}\frac{1}{4\pi\varepsilon_0}\frac{Z_\alpha Z_\beta e^2}{|\vec{R_\alpha}-\vec{R_\beta}|} - \sum_{\alpha=1}^{N}\sum_{i=1}^{n_e}\frac{1}{4\pi\varepsilon_0}\frac{Z_\alpha e^2}{|\vec{R_\alpha}-\vec{r_i}|},\end{aligned} \tag{1.1.1}$$

where $\hat{H}_e(\vec{r},\vec{R})$ stands for the electronic Hamiltonian, and its variables, $\vec{r_i}$ and $\vec{R_\alpha}$ are the positions of the ith electron and αth nuclei in the molecular system. $\nabla^2_{r_i}$ and $\nabla^2_{R_\alpha}$ are the second-order derivatives with respect to these ($\vec{r_i}$ and $\vec{R_\alpha}$) coordinates, respectively. $\hbar$ and ε_0 stand for the constant of the reduced Planck's and the vacuum permittivity. $Z_\alpha e$ is a charge of the αth nuclei.

Generally, the mass of the nuclei is heavy compared to that of the electron, which means that the light electron can move more rapidly than heavy

nuclei. The BOA [1, 2] is based on this theory, and it allows us to simplify the TI Schrödinger equation to solve the nuclear and the electronic motions separately. The system's total wave function in the Born-Oppenheimer framework can be formulated as a product of the electronic and nuclear wave functions, namely

$$\Psi(\vec{r}, \vec{R}) = \psi(\vec{r}, \vec{R}) \cdot \phi(\vec{R}). \tag{1.1.2}$$

Here, the electronic wave function $\psi(\vec{r}, \vec{R})$ depends on both the electronic ($\vec{r}$) and nuclear ($\vec{R}$) coordinates, whereas the nuclear wave function $\phi(\vec{R})$ relies on only the nuclear ($\vec{R}$) coordinates. From now on, I will use atomic units because of convenience; that is, $\hbar = m_e = e = \frac{1}{4\pi\varepsilon_0} = 1$ atomic unit (or au for a short form).

By taking into account the Born-Oppenheimer Hamiltonian (eq. 1.1.1) and its total wave function (eq. 1.1.2), the time-independent Schrödinger equation (TISE) takes the following form

$$\begin{aligned} \hat{H}\Psi(\vec{r}, \vec{R}) &= \left[\hat{T}_N + \hat{T}_e + V_{ee} + V_{NN} + V_{eN}\right] \psi(\vec{r}, \vec{R}) \cdot \phi(\vec{R}) \\ &= \left[\hat{T}_N\right] \psi(\vec{r}, \vec{R}) \cdot \phi(\vec{R}) + \left[\hat{H}_e\right] \psi(\vec{r}, \vec{R})\phi(\vec{R}) \\ &= E\psi(\vec{r}, \vec{R}) \cdot \phi(\vec{R}). \end{aligned} \tag{1.1.3}$$

Let's calculate the nuclear kinetic operator term in eq 1.1.3 with the total wave function,

$$\begin{aligned} \hat{T}_N\psi(\vec{r}, \vec{R}) \cdot \phi(\vec{R}) &= -\sum_{\alpha=1}^{N} \frac{1}{2M_\alpha} \nabla^2_{R_\alpha} \psi(\vec{r}, \vec{R}) \cdot \phi(\vec{R}) \\ = \psi(\vec{r}, \vec{R})\hat{T}_N\phi(\vec{R}) &- \sum_{\alpha=1}^{N} \frac{1}{2M_\alpha} \Gamma(\psi, \phi), \end{aligned} \tag{1.1.4}$$

where the $\Gamma(\psi, \phi)$ contains the non-adiabatic coupling terms, expressing non-adiabatic effects between the electronic states in a molecule: $\Gamma(\psi, \phi) =$

$\phi(\vec{R})\nabla^2_{R_\alpha}\psi(\vec{r},\vec{R}) + 2\cdot\left(\nabla_{R_\alpha}\psi(\vec{r},\vec{R})\right)\cdot\left(\nabla_{R_\alpha}\phi(\vec{R})\right)$. On the other hand, if we multiply equation 1.1.3 by $\psi(\vec{r},\vec{R})$ on the left-hand side and compute the integral of the electronic coordinates, the term $(\Gamma(\psi,\phi))$ can have two parts (in matrix form) [7]:

$$\Gamma(\psi,\phi)_{ji} = 2\tau^{(1)}_{ji}\cdot\nabla_{R_\alpha}\phi(\vec{R}) + \tau^{(2)}_{ji}\phi(\vec{R}), \tag{1.1.5}$$

containing the non-adiabatic coupling vector $(\tau^{(1)}_{ji})$ and non-adiabatic coupling scalar $(\tau^{(2)}_{ji})$ terms in matrix forms,

$$\tau^{(1)}_{ji} = \langle\psi_j(\vec{r},\vec{R})|\nabla_{R_\alpha}\psi_i(\vec{r},\vec{R})\rangle = \frac{\langle\psi_j(\vec{r},\vec{R})|\nabla_{R_\alpha}\vec{H}_e|\psi_i(\vec{r},\vec{R})\rangle}{V_i - V_j} \tag{1.1.6}$$

and

$$\tau^{(2)}_{ji} = \langle\psi_j(\vec{r},\vec{R})|\nabla^2_{R_\alpha}\psi_i(\vec{r},\vec{R})\rangle = (\nabla_{R_\alpha}\tau^{(1)})_{ji} + (\tau^{(1)}\tau^{(1)})_{ji}, \tag{1.1.7}$$

respectively. The $\Gamma(\psi,\phi)$ terms couple the system's electronic and nuclear motions. If $\Gamma(\psi,\phi)$ are neglected due to their very small value compared to the $\psi(\vec{r},\vec{R})\hat{T}_N\phi(\vec{R})$, the Born-Oppenheimer approximation perfectly works. In this representation, the nuclear and electronic motions can be decoupled, and the nuclei move on a single electronic potential energy surface. Thus, in the Born-Oppenheimer approximation equation 1.1.3 gives the following 1.1.9 form by considering the condition of

$$\hat{T}_N\psi(\vec{r},\vec{R})\cdot\phi(\vec{R}) \approx \psi(\vec{r},\vec{R})\hat{T}_N\phi(\vec{R}), \tag{1.1.8}$$

$$\begin{aligned}\hat{H}\psi(\vec{r},\vec{R})\phi(\vec{R}) &= \psi(\vec{r},\vec{R})\hat{T}_N\phi(\vec{R}) + \hat{H}_{el}\psi(\vec{r},\vec{R})\phi(\vec{R}) \\ &= \psi(\vec{r},\vec{R})\left[\hat{T}_N\phi(\vec{R})\right] + \left[\hat{H}_e\psi(\vec{r},\vec{R})\right]\phi(\vec{R}) \\ &= E\psi(\vec{r},\vec{R})\phi(\vec{R}).\end{aligned} \tag{1.1.9}$$

Equation 1.1.9 can be solved for the electronic and nuclear motions indi-

vidually. First, let's write TISE for the electronic DOFs by ignoring the nuclear motion ($M_\alpha >> m_e$ or $\hat{T}_e >> \hat{T}_N$) due to its very slow magnitude of motion compared with the electronic motion

$$\hat{H}_e\psi(\vec{r},\vec{R}) = E\psi(\vec{r},\vec{R}) = E_{e_i}(R)\psi_i(\vec{r},\vec{R}). \tag{1.1.10}$$

This equation is just an eigenvalue problem that is not related to the time, where $E_{e_i}(R)$ is eigenvalues for a set of fixed geometry $\vec{R}$ of nuclei. After obtaining each electronic energy ($E_{e_i}(R)$) for certain points of $\vec{R}$, we can move on to solve the system's nuclear motion by putting the values of $E_{e_i}(R)$ into the eq. 1.1.9; that is,

$$\begin{aligned}\hat{H}\psi_i(\vec{r},\vec{R})\phi(\vec{R}) &= \psi_i(\vec{r},\vec{R})\left[\hat{T}_N\phi(\vec{R})\right] + E_{e_i}(R)\psi_i(\vec{r},\vec{R})\phi(\vec{R}) \\ &= E\psi_i(\vec{r},\vec{R})\phi(\vec{R})\end{aligned} \tag{1.1.11}$$

or

$$\hat{T}_N\phi(\vec{R}) + E_{e_i}(R)\phi(\vec{R}) = E\phi(\vec{R}) = E_{N_i}\phi(\vec{R}). \tag{1.1.12}$$

Equation 1.1.12 gives the eigenenergies E_{N_i} for the nuclear motion using the values of eigenenergies ($E_{e_i}(R)$) of the electronic motion.

In the BOA, the electronic and nuclear motions are solved independently using equations 1.1.8 and 1.1.9 by neglecting the non-adiabatic coupling terms ($\Gamma(\psi,\phi) \approx 0$). However, there is a limit to this approximation; whenever the electronic states get closer to each other or cross one another, the magnitude of the $\Gamma(\psi,\phi)$ becomes significantly large. This is because the NACTs are inversely proportional to the differences in energy levels between corresponding electronic states (see equations 1.1.6 and 1.1.7). Therefore, we cannot omit the $\Gamma(\psi,\phi)$ terms because of the significant contributions; thus, the Born-Oppenheimer model does not work at all in such cases.

1.2 Molecular electronic structure methods

Electronic structure calculations are used to investigate the electronic features of molecules. These calculations provide valuable insights into the characteristics of electrons within molecular systems, allowing us to understand and predict molecular properties such as geometry, electronic energy states, dipole moments, etc.

Potential energy surfaces (PESs), PDM, and transition dipole moment (TDM) dependent on nuclear coordinates can be obtained by solving the time-independent form of the electronic Schrödinger equation (described in eq. 1.1.10). This field is called electronic structure theory, in which computer programs such as Molpro [35, 36] can make calculations. These electronic structure data (PESs, PDMs, TDMs and so forth...) can be employed to study nuclear dynamics (which will be detailed in section 1.6). A primary difficulty in quantum chemistry is that the Schrödinger equation cannot be solved precisely due to the electron-electron interaction term present in the Hamiltonian (in eq. 1.1.1). Quantum-chemical methods search for approximate and reasonable solutions to the equation, employing various computational methods. Both the eigenvalues and eigenfunctions depend on the type of applied method of the electronic structure calculations.

In accordance with the number of configurations employed to construct the reference wave function, the ab initio calculations might be classified into two categories: single-configuration and multi-configurational methods [41]. The single-configuration cases are usually based on the single Hartree–Fock reference determining the system's optimal lowest energy state and molecular orbital arrangement. Post-HF methods introduce the electron correlation, usually coupled-cluster or perturbative Møller–Plesset levels at the configuration interaction. In the multi-configurational methods, the electronic correlation is already incorporated in the reference wave function by using a multi-configurational self-consistent-field (MCSCF) wave

function, multi-reference configuration interaction (MRCI), multi-reference coupled-cluster (MRCC) or multi-reference perturbative Møller–Plesset (MRPT) techniques, which can determine a set of molecular orbitals. The primary benefit of the multi-configurational approaches is that we can deal with many ranges of applicability, for example, ground as well as excited states, and transition between electronic states, which we cannot calculate in the single-reference methods.

In the following subsection, we will discuss the multi-reference configuration interaction (MRCI) method (which is multi-configurational) and the related wave function of the electronic motion. I used this method in the calculations with the Molpro quantum package for the NaH system. This method is chosen to calculate the electronic structure calculations because it can involve considering all states (including excited states) simultaneously by combining truncated configurations from all reference states. Moreover, this approach is highly accurate and can give us an accurate depiction of degeneracies (ACs and CIs), for example, in the non-adiabatic phenomenon.

1.2.1 Multi-reference configuration interaction

Because the Hartree-Fock (HF) approach cannot give us the exact solutions in many cases due to its only single determinant, I will start with a more accurate method, the multi-reference configuration interaction method used during my calculations for the NaH system. In the HF approximation, the electrons are repelled by the mean fields if two of the electrons correlate their motions to each other, resulting in a lowering of energy, which is part of the correlation energy. Unlike the HF method, where each electron interacts with the average field created by all remaining electron impacts, the MRCI considers the electron correlation interactions between electrons

in a many-electron system. Thus, the multi-reference configuration interaction [42] is one of the simplest and most effective methods to calculate the electron correlation in many-electron systems. The energy of electron correlation due to the correlated (not independent) motion of electrons can be formulated as the contrast between the system's exact (or true) nonrelativistic energy (E_{ex}) and the HF energy (E_{HF})

$$E_{corr} = E_{ex} - E_{HF}. \tag{1.2.1}$$

Electron correlation might be classified into dynamical and static (non-dynamical) electron correlations [43]. In dynamic electron correlation, the correlation between the spatial position of electrons with opposite spin due to their Coulomb repulsion is not considered. In contrast, in static correlation, the electronic state can be well described only with more than one degenerate determinants. This type of electron correlation is known as near-degeneracy correlation, which arises from electronic configurations' near-degeneracy cases, including conical intersections and avoided crossings. The MRCI method can simultaneously consider dynamical and static electron correlations, which suits my research area related to non-adiabatic phenomena.

As for the wave function of the MRCI approach, it cannot be expressed as one Slater (or HF) determinant, but it can be obtained by a linear combination of an infinite number of Slater determinants [42]:

$$|\Phi_0\rangle = c_0|\Psi_0\rangle + \sum_{a,r} c_a^r|\Psi_a^r\rangle + \sum_{\substack{a<b\\r<s}} c_{ab}^{rs}|\Psi_{ab}^{rs}\rangle + \sum_{\substack{a<b<c\\r<s<t}} c_{abc}^{rst}|\Psi_{abc}^{rst}\rangle + ..., \tag{1.2.2}$$

where the a, b, c, ... stand for occupied orbitals, while r, s, t, ... label virtual orbitals in the many-electron determinants. c_0, c_a^r, c_{ab}^{rs}, c_{abc}^{rst} ... are the expansion coefficients. $|\Psi_0\rangle$, $|\Psi_a^r\rangle$, $|\Psi_{ab}^{rs}\rangle$ and $|\Psi_{abc}^{rst}\rangle$ wave functions define the (one-electron) HF, singly, doubly and triply excited determinants, respectively. If we have some arbitrary 2K spin orbitals, N will be occupied

in $|\Psi_0\rangle$, while 2K-N will be unoccupied. In this case, we can construct different $\binom{2K}{N}$ N-electron Slater determinants, which are extremely large numbers of Slater determinants, even for small systems to be calculated. Therefore, the full (configuration interaction) wave function (1.2.2) has to be truncated.

The system's exact nonrelativistic energy, where its full configuration interaction wave function described in eq 1.2.2 can be defined as

$$\hat{H}|\Phi_0\rangle = E_{ex}|\Phi_0\rangle. \tag{1.2.3}$$

Here, the $\hat{H}$ is referred to as the electron Hamiltonian discussed in the previous section. The linear variation principle is one of the best possible ways to get the electron correlation energy in the configuration interaction method. Thus, equation 1.2.2 has to be multiplied first by $|\Psi_0\rangle$, then by $|\Psi_a^r\rangle$, then $|\Psi_{ab}^{rs}\rangle$ etc. Equation 1.2.3 can be rewritten after the multiple multiplications:

$$(\hat{H} - E_{HF})|\Phi_0\rangle = (E_{ex} - E_{HF})|\Phi_0\rangle = E_{corr}|\Phi_0\rangle. \tag{1.2.4}$$

This equation 1.2.4 can also make it difficult to calculate if all possible excitation Slater determinants are included as in equation 1.2.2. As discussed above, this equation also might be truncated along with eq. 1.2.2, and usually reasonable truncation can be obtained by considering single and double excitations. Single excitations and ground state are not coupled, so $\langle\Psi_0|\hat{H}|\Psi_a^r\rangle = 0$. Additionally, the triples and quadruples do not mix directly with $|\Psi_0\rangle$; therefore, these couplings can be expected to contribute very little to the ground state energy. All the above is considered, the above equations can be rewritten for the electron correlations and the full

configuration interaction in truncated versions:

$$\sum_{\substack{c<d \\ t<u}} c_{cd}^{tu} \langle \Psi_0 | \hat{H} | \Psi_{cd}^{tu} \rangle = E_{corr} \tag{1.2.5}$$

and

$$\langle \Psi_{ab}^{rs} | \hat{H} | \Psi_0 \rangle + \sum_{\substack{c<d \\ t<u}} c_{cd}^{tu} \langle \Psi_{ab}^{rs} | (\hat{H} - E_{HF}) | \Psi_{cd}^{tu} \rangle = c_{ab}^{rs} E_{corr}, \tag{1.2.6}$$

respectively. By using the truncations, we can determine the electron correlation energy more easily, the so-called double configuration interaction variant of the full CI method:

$$E_{corr} \cong - \sum_{\substack{a<b \\ r<s}} \frac{\langle \Psi_0 | \hat{H} | \Psi_{ab}^{rs} \rangle \langle \Psi_{ab}^{rs} | \hat{H} | \Psi_0 \rangle}{\langle \Psi_{ab}^{rs} | (\hat{H} - E_{HF}) | \Psi_{ab}^{rs} \rangle} = \sum_{\substack{a<b \\ r<s}} E_{corr} \begin{pmatrix} rs \\ ab \end{pmatrix}, \tag{1.2.7}$$

where the notation $E_{corr} \begin{pmatrix} rs \\ ab \end{pmatrix}$ expresses the contribution of the double excitation of the correlation energy. The notation $\begin{pmatrix} rs \\ ab \end{pmatrix}$ has been introduced in the reference [42], meaning the double excitation ($|\Psi_{ab}^{rs}\rangle$) because it has two virtual orbitals (rs) and two occupied orbitals (ab).

So, the MRCI approach is one of the most accurate methods to get electronic structure data by considering all states, and at the same time by combining contracted configurations from all reference states. In contrast to the HF method, we can involve electron-electron interaction by calculating electron correlation energy in a truncated way.

1.3 Adiabatic versus diabatic representations

We discussed in the earlier section that the Born-Oppenheimer assumes that the electronic and nuclear motions are decoupled, allowing us to treat these motions separately. On the other hand, it has been shown that two or more electronic states can get closer to each other or even intersect in polyatomic systems [19, 22], and they are named avoided crossing (AC) and conical intersection (CI), respectively. In the case of AC or CI in the system, the electronic states are strongly coupled to each other, and we should take into account the non-adiabatic coupling terms (in equation 1.1.5). For a simple two-level system, the adiabatic Hamiltonian takes the following form:

$$\hat{H}_{adi} = \begin{pmatrix} \hat{T}_N + \tau_{11} & \tau_{12} \\ \tau_{21} & \hat{T}_N + \tau_{22} \end{pmatrix} + \begin{pmatrix} W_1 & 0 \\ 0 & W_2 \end{pmatrix} \tag{1.3.1}$$

where $\hat{T}_N$ is the nuclear kinetic energy operator (eq. 1.1.8), and τ_{ij} are the non-adiabatic (vector) coupling terms (eq. 1.1.6). W_1 and W_2 are the adiabatic potential energy surfaces calculated in the framework of the Born–Oppenheimer. In the *adiabatic* model, all the coupling matrix elements through potential energies are zero (off-diagonal elements of the second term in equation 1.3.1), and the coupling between different electronic states occurs through the nuclear kinetic energy terms. As we see, the Born–Oppenheimer treatment leads to the adiabatic framework, in which the non-adiabatic (matrix) terms are responsible for the coupling between adiabatic states through the nuclear kinetic operators. However, the main disadvantage of this adiabatic treatment is that calculating the non-adiabatic coupling terms (τ_{ij}) along with the kinetic energy operators brings difficulty in computational simulations since the nuclear kinetic energy operator ($\hat{T}_N$) contains derivatives. Therefore, expressing the non-adiabatic coupling terms in the potential energy matrix rather than the

kinetic energy matrix is convenient. In order to transfer the non-adiabatic coupling terms from the kinetic energy operator into potential energy, we can use a transformation operator called adiabatic-to-diabatic transformation (ADT). For a two-state system, it can be expressed as:

$$\hat{U}_{ADT} = \begin{pmatrix} \cos\gamma(\vec{R}) & \sin\gamma(\vec{R}) \\ -\sin\gamma(\vec{R}) & \cos\gamma(\vec{R}) \end{pmatrix}, \tag{1.3.2}$$

where $\cos\gamma(\vec{R})$ and $\sin\gamma(\vec{R})$ can be defined as follows:

$$\sin\gamma(R) = \frac{V_{12}}{\sqrt{\Delta^2 + V_{12}^2}} \tag{1.3.3}$$

$$\cos\gamma(R) = \frac{V_{11} - V_{22}}{2\sqrt{\Delta^2 + V_{12}^2}}. \tag{1.3.4}$$

Here, $\gamma(\vec{R})$ is the ADT angle that depends on the nuclear geometry ($\vec{R}$). V_{11} and V_{22} are the diabatic potential energy surfaces, while V_{12} (or V_{21} in equation 1.3.5) is the coupling term transformed from adiabatic to diabatic representation. The notation $\Delta = \frac{1}{2}(V_{11} - V_{22})$ is introduced to get a compact form. After the transformation is performed, the *diabatic* Hamiltonian can be obtained as:

$$\hat{H}_{dia} = \hat{T}_N.\hat{1} + \begin{pmatrix} V_{11} & V_{12} \\ V_{21} & V_{22} \end{pmatrix}, \tag{1.3.5}$$

where $\hat{1}$ is the two-dimensional unit matrix. Due to this transformation, the diabatic potential energy matrix has not only diagonal elements but also non-zero off-diagonal elements. The derivative coupling (in the nuclear kinetic energy matrix) cannot vanish completely for every nuclear geometry ($\vec{R}$), but it can become negligibly small.

In the diabatic picture, not only the Hamiltonian matrix but also the electron-nuclear wave functions have to change their forms using the ADT

described in equation 1.3.2

$$\begin{cases} \psi^{dia}(\vec{r},\vec{R}) = \hat{U}^{\dagger}_{ADT}\psi^{adi}(\vec{r},\vec{R}) \\ \phi^{dia}(\vec{R}) = \hat{U}_{ATD}\phi^{adi}(\vec{R}), \end{cases} \tag{1.3.6}$$

or

$$\begin{cases} \begin{pmatrix} \psi_1^{dia}(\vec{r},\vec{R}) \\ \psi_2^{dia}(\vec{r},\vec{R}) \end{pmatrix} = \begin{pmatrix} \cos\gamma(\vec{R}) & -\sin\gamma(\vec{R}) \\ \sin\gamma(\vec{R}) & \cos\gamma(\vec{R}) \end{pmatrix} \begin{pmatrix} \psi_1^{adi}(\vec{r},\vec{R}) \\ \psi_2^{adi}(\vec{r},\vec{R}) \end{pmatrix} \\ \begin{pmatrix} \phi_1^{dia}(\vec{R}) \\ \phi_2^{dia}(\vec{R}) \end{pmatrix} = \begin{pmatrix} \cos\gamma(\vec{R}) & \sin\gamma(\vec{R}) \\ -\sin\gamma(\vec{R}) & \cos\gamma(\vec{R}) \end{pmatrix} \begin{pmatrix} \phi_1^{adi}(\vec{R}) \\ \phi_2^{adi}(\vec{R}) \end{pmatrix}. \end{cases} \tag{1.3.7}$$

For the two-state system in matrix form, the indexes (1 and 2) in the wave functions express the number of states. The modified wave functions, $\psi^{dia}(\vec{r},\vec{R})$ and $\phi^{dia}(\vec{R})$, are related to the diabatic electronic and nuclear motions, while the $\psi^{adi}(\vec{r},\vec{R})$ and $\phi^{adi}(\vec{R})$ are adiabatic electronic and nuclear wave functions, respectively. Thus, we can express electronic and nuclear motions in adiabatic and diabatic pictures. The diabatic expressions are very common in the investigation of non-adiabatic nuclear dynamics.

1.4 Conical intersection in molecular systems

Conical intersections do not exist as isolated points in space; instead, they comprise an infinite number of connected points forming the seam [22]. Conical intersections are degeneracy between potential energy surfaces in a molecular system at a particular internuclear coordinate. Non-adiabatic phenomena describe the concepts of conical intersections where the BOA does not hold. It has been shown that non-adiabatic processes usually occur on a femtosecond timescale [22, 44]. The adiabatic picture is widely used

to study the non-adiabatic nuclear dynamics in molecules. The adiabatic potential (W) can be obtained using the ADT operator [19, 22]

$$W = \hat{U}_{ADT} V \hat{U}^{\dagger}_{ADT} \quad (\text{or} \quad V = \hat{U}^{\dagger}_{ADT} W \hat{U}_{ADT}). \tag{1.4.1}$$

Here, the lower (W_1) and upper (W_2) adiabatic potential energies for a two-level system can be taken by diagonalizing the diabatic potential (V) matrix:

$$W_{1,2} = \frac{1}{2}(V_{11} + V_{22}) \pm \frac{1}{2}\sqrt{(V_{11} - V_{22})^2 + 4V_{12}^2}, \tag{1.4.2}$$

where $W_{1,2}$ and V_{ij} are the adiabatic and diabatic potential energies (the matrix forms of them are given in equations 1.3.1 and 1.3.5), respectively. If we introduce notation, $\Sigma = \frac{1}{2}(V_{11}+V_{22})$, and consider Δ (described in the previous section), the equation 1.4.2 can be expressed in a compact form, that is,

$$W_{1,2} = \Sigma \pm \sqrt{\Delta^2 + V_{12}^2}. \tag{1.4.3}$$

We can define the conical intersection in adiabatic representation by using equation 1.4.3. In a two-level system, the upper and lower adiabatic potential energies degenerate at a particular nuclear geometry ($\vec{R}$) whenever the condition $W_2 = W_1$ is fulfilled. In the case of eq. 1.4.3, we can get the two conditions to attain the degeneracy condition by making both terms under the square root zero,

$$\begin{cases} V_{11} = V_{22} \\ V_{12} = 0. \end{cases} \tag{1.4.4}$$

These two conditions in eq. 1.4.4 are satisfied in a $N^{int} - 2$ subspace (or seam space), where N^{int} stands for internal nuclear coordinate came from $N^{int} = 3N-5$ (N is the number of atoms in the molecule) for diatomic and $N^{int} = 3N-6$ for polyatomic molecules. For a diatomic molecule with only one degree of freedom ($N^{int} = 1$), it is not possible for two electronic states having the same symmetry to become degenerate (except in rare cases),

and this restriction is typically named the noncrossing rule in the literature [22].

According to the symmetry type, conical intersections can be classified into the following categories: symmetry-required and symmetry-allowed (or different symmetry) [22]. In the former case, conical intersections in molecules can occur when the two electronic states hold the same symmetry (or the same multiplicity defined as 2S+1, where S is the total spin angular momentum). The requirements for degeneracy (equation 1.4.4) are satisfied by symmetry alone. In the symmetry-allowed conical intersection case, the symmetries of intersections are not required to be the same. One of the requirements is that $V_{12} = 0$ is satisfied by symmetry, while the second one ($V_{11} = V_{22}$) is satisfied in a subspace of dimension $N^{int} - 1$. In some literature, an accidental conical intersection can occur in some molecules in nature that have little or no symmetry. Yet, this topic is beyond the scope of this Thesis.

Conical intersections can play an essential role in the photophysics, photochemistry and spectroscopy of molecular systems, especially when the ground state is one of the intersecting states. Conical intersections can be used to explain the mechanism of non-adiabatic processes in molecular systems.

1.5 Light-matter interaction within classical electromagnetic and quantized fields

The light-matter interaction appears when molecular systems are placed in an applied external field. External fields and the resulting light-matter interaction (between light and a molecule) are pivotal in exploring light-induced non-adiabatic features in molecules. I will give general explana-

tions of two types of external fields used to study some molecular systems' properties.

A. Classical approach

Let's first start with the classical electromagnetic (EM) field, which includes electric ($\vec{\mathbf{E}}(\mathbf{r},t)$) and magnetic ($\vec{\mathbf{B}}(\mathbf{r},t)$) fields satisfying the Maxwell's equations [29, 45]:

$$\vec{\mathbf{E}}(\mathbf{r},t) = -\frac{1}{c}\frac{\partial}{\partial t}\vec{\mathbf{A}}(\mathbf{r},t) \tag{1.5.1}$$

and

$$\vec{\mathbf{B}}(\mathbf{r},t) = \nabla \times \vec{\mathbf{A}}(\mathbf{r},t), \tag{1.5.2}$$

where $\vec{\mathbf{A}}(\mathbf{r},t)$ expresses a vector potential that can be defined as a linear superposition of plane waves ($k = \omega_{\mathbf{k}}/c$),

$$\vec{\mathbf{A}}(\mathbf{r},t) = \sum_{\mathbf{k}\lambda} \hat{\mathbf{e}}_{\mathbf{k}\lambda} \left[A_{\mathbf{k}\lambda} e^{i(\mathbf{k}\cdot\mathbf{r}-\omega_{\mathbf{k}}t)} + A^{*}_{\mathbf{k}\lambda} e^{-i(\mathbf{k}\cdot\mathbf{r}-\omega_{\mathbf{k}}t)} \right]. \tag{1.5.3}$$

Here, $\hat{\mathbf{e}}_{\mathbf{k}\lambda}$ indicates the linear polarization (vector), which depends on the wave (or propagation) vector, where $\mathbf{k} = \frac{2\pi}{\lambda}$. $A_{\mathbf{k}\lambda}$ is a constant amplitude of the real $\vec{\mathbf{A}}(\mathbf{r},t)$ vector for the mode $\mathbf{k}\lambda$, and $\omega_{\mathbf{k}}$ is the angular frequency of the EM field. By considering equation 1.5.3, the electric field (eq. 1.5.1) can be rewritten in the form

$$\begin{aligned} \vec{\mathbf{E}}(\mathbf{r},t) &= -\frac{1}{c}\frac{\partial}{\partial t}\vec{\mathbf{A}}(\mathbf{r},t) \\ &= \frac{i}{c}\sum_{\mathbf{k}\lambda} \omega_{\mathbf{k}} \hat{\mathbf{e}}_{\mathbf{k}\lambda} \left[A_{\mathbf{k}\lambda} e^{i(\mathbf{k}\cdot\mathbf{r}-\omega_{\mathbf{k}}t)} - A^{*}_{\mathbf{k}\lambda} e^{-i(\mathbf{k}\cdot\mathbf{r}-\omega_{\mathbf{k}}t)} \right]. \end{aligned} \tag{1.5.4}$$

If the vector product of three elements is considered

$$\nabla \times (\phi\vec{\mathbf{A}}) = \nabla\phi \times \vec{\mathbf{A}} + \phi\nabla \times \vec{\mathbf{A}}, \tag{1.5.5}$$

and if we apply this to our case, we will get the following equation

$$\nabla \times A_{\mathbf{k}\lambda} e^{i(\mathbf{k}\cdot\mathbf{r}-\omega_{\mathbf{k}}t)}\hat{\mathbf{e}}_{\mathbf{k}\lambda} = \nabla A_{\mathbf{k}\lambda} e^{i(\mathbf{k}\cdot\mathbf{r}-\omega_{\mathbf{k}}t)} \times \hat{\mathbf{e}}_{\mathbf{k}\lambda} + A_{\mathbf{k}\lambda} e^{i(\mathbf{k}\cdot\mathbf{r}-\omega_{\mathbf{k}}t)} \nabla \times \hat{\mathbf{e}}_{\mathbf{k}\lambda}. \quad (1.5.6)$$

The second term of equation 1.5.6 vanishes due to the constants $A_{\mathbf{k}\lambda}$ and $\hat{\mathbf{e}}_{\mathbf{k}\lambda}$:

$$\nabla \times A_{\mathbf{k}\lambda} e^{i(\mathbf{k}\cdot\mathbf{r}-\omega_{\mathbf{k}}t)}\hat{\mathbf{e}}_{\mathbf{k}\lambda} = A_{\mathbf{k}\lambda} \nabla e^{i(\mathbf{k}\cdot\mathbf{r}-\omega_{\mathbf{k}}t)} \times \hat{\mathbf{e}}_{\mathbf{k}\lambda} = i\frac{\omega_{\mathbf{k}}}{c} A_{\mathbf{k}\lambda} e^{i(\mathbf{k}\cdot\mathbf{r}-\omega_{\mathbf{k}}t)} \hat{\mathbf{k}} \times \hat{\mathbf{e}}_{\mathbf{k}\lambda}. \quad (1.5.7)$$

By considering the above equation, we can obtain the magnetic part of the EM field using the vector potential in the following form

$$\begin{aligned} \vec{\mathbf{B}}(\mathbf{r},t) &= \nabla \times \vec{\mathbf{A}}(\mathbf{r},t) \\ &= \frac{i}{c} \sum_{\mathbf{k}\lambda} \omega_{\mathbf{k}} (\hat{\mathbf{k}} \times \hat{\mathbf{e}}_{\mathbf{k}\lambda}) \left[A_{\mathbf{k}\lambda} e^{i(\mathbf{k}\cdot\mathbf{r}-\omega_{\mathbf{k}}t)} - A^*_{\mathbf{k}\lambda} e^{-i(\mathbf{k}\cdot\mathbf{r}-\omega_{\mathbf{k}}t)} \right]. \end{aligned} \quad (1.5.8)$$

Using Euler's formula, $\cos(\mathbf{k}\cdot\mathbf{r}-\omega_{\mathbf{k}}t) = \frac{1}{2}\left(e^{\mathbf{k}\cdot\mathbf{r}-\omega_{\mathbf{k}}t} - e^{-\mathbf{k}\cdot\mathbf{r}+\omega_{\mathbf{k}}t}\right)$, and $e^{i\pi}+1 = 0$ (or $i = e^{i\pi/2}$), equations 1.5.4 and 1.5.8 can be simplified for the classical EM radiation case.

The total energy of the classical electromagnetic field ($\hat{H}^{CM}_{field}$) in volume V is equal to the sum of the electric and magnetic energy parts:

$$\hat{H}^{CM}_{field} = \frac{1}{2} \int_V dV \left[\epsilon_0 \vec{\mathbf{E}}^2(\mathbf{r},t) + \frac{1}{\mu_0} \vec{\mathbf{B}}^2(\mathbf{r},t) \right], \quad (1.5.9)$$

where ϵ_0 and μ_0 are the vacuum permittivity and magnetic constant, respectively. The total Hamiltonian ($\hat{H}^{CM}_{tot}$) takes the following parts in the case of an external classical EM field [46, 47]:

$$\hat{H}^{CM}_{tot} = \hat{H}_{mol} + \hat{H}^{CM}_{int}, \quad (1.5.10)$$

where the term $\hat{H}_{mol}$ indicates the Hamiltonian corresponding to the zero-order molecule, which includes the PESs and kinetic energy operators. The

last term ($\hat{H}_{int}^{CM}$) is the time-dependent interaction term between a molecular system and the EM field.

B. Quantum approach: Fock states

As for the quantized EM field, all vector quantities should be expressed as operators. The Fock space can be used to depict the confined photonic mode of a cavity [46, 48]. Fock states can describe the quantum states of systems with a variable number of particles, such as photons, in the case of the quantized EMs. In Fock states, ladder operators serve to destroy or create photons in the system:

$$\hat{a}_{\mathbf{k}\lambda} = \frac{1}{\sqrt{2m\omega_{\mathbf{k}}\hbar}}(m\omega_{\mathbf{k}}\hat{x}_{\mathbf{k}\lambda} + i\hat{p}_{\mathbf{k}\lambda}) \tag{1.5.11}$$

$$\hat{a}_{\mathbf{k}\lambda}^{\dagger} = \frac{1}{\sqrt{2m\omega_{\mathbf{k}}\hbar}}(m\omega_{\mathbf{k}}\hat{x}_{\mathbf{k}\lambda} - i\hat{p}_{\mathbf{k}\lambda}), \tag{1.5.12}$$

where $\hat{x}_{\mathbf{k}\lambda}$ and $\hat{p}_{\mathbf{k}\lambda}$ stand for the unit-less photon displacement (or position) coordinate and momentum operators, respectively, while m is the mass unity ($m = 1$ in atomic unit).

When the ladder operators act on the quantum state $|n_{\mathbf{k}\lambda}\rangle$, the lowering operator $\hat{a}_{\mathbf{k}\lambda}$ can annihilate photons, while the raising operator $\hat{a}_{\mathbf{k},\lambda}^{\dagger}$ creates photons in the system:

$$\hat{a}_{\mathbf{k}\lambda}|n_{\mathbf{k}\lambda}\rangle = \sqrt{n_{\mathbf{k}\lambda}}|n_{\mathbf{k}\lambda} - 1\rangle, \tag{1.5.13}$$

$$\hat{a}_{\mathbf{k}\lambda}^{\dagger}|n_{\mathbf{k}\lambda}\rangle = \sqrt{n_{\mathbf{k}\lambda} + 1}|n_{\mathbf{k}\lambda} + 1\rangle. \tag{1.5.14}$$

Here, the quantum state $|n_{\mathbf{k}\lambda}\rangle$ is named the Fock state, indicating the number of photons applied to the system (n=0,1,2,3,...). The lowering operator, $\hat{a}_{\mathbf{k}\lambda}$ acting on $|n_{\mathbf{k}\lambda}\rangle$ quantum (or Fock) state, decreases the photon number by one photon. Hence, the eigenvalue energy of the system will be reduced by $\hbar\omega_{\mathbf{k}}$, changing the quantum state from $|n_{\mathbf{k}\lambda}\rangle$ to $|n_{\mathbf{k}\lambda} - 1\rangle$. As to the raising operator, $\hat{a}_{\mathbf{k}\lambda}^{\dagger}$, it increases the photon number (as well as the

eigenvalue energy of the system) by one photon and modifies the quantum state from $|n_{\mathbf{k}\lambda}\rangle$ to $|n_{\mathbf{k}\lambda}+1\rangle$. The total Hamiltonian in the Fock-space-based quantum state can be written in the form [46, 47]:

$$\begin{aligned}\hat{H}_{tot}^{fock} =& \hat{H}_{mol} + \hat{H}_{field}^{fock} + \hat{H}_{int} \\ =& \hat{H}_{mol} + \hbar\omega_{\mathbf{k}}\hat{a}_{\mathbf{k}\lambda}^{\dagger}\hat{a}_{\mathbf{k}\lambda} - g\hat{\vec{\mu}}\hat{\mathbf{e}}_{\mathbf{k}\lambda}(\hat{a}_{\mathbf{k}\lambda}^{\dagger} + \hat{a}_{\mathbf{k}\lambda}),\end{aligned} \tag{1.5.15}$$

where g is the coupling strength.

The general form of the interaction term for both classical and quantized EM fields can be expressed as a scalar product of the applied EM field and the molecule's dipole moment. Understanding the properties of molecular systems in the presence of external fields is crucial for various applications. In the following chapters, I will discuss some of these properties in detail.

1.6 Nuclear dynamics

In molecular dynamics, the purpose is to solve the time-dependent Schrödinger equation (TDSE) for the motion of nuclei. In general, the TDSE for the nuclear motion can be written [38] as:

$$\hat{H}\phi(\vec{R},t) = i\hbar\frac{\partial\phi(\vec{R},t)}{\partial t}, \tag{1.6.1}$$

where the nuclear wave function $\phi(\vec{R},t)$ and the Hamiltonian ($\hat{H}$) are time-dependent instead of TI. Unlike quantum chemistry calculations, molecular quantum dynamics is complex and numerically demanding. Generally, the time-dependent solutions are more intuitive, connecting directly with the motion of the system. As discussed in the previous section, external fields such as laser pulses or optical cavities can be added to the total Hamiltonian (see equations 1.5.10 or 1.5.15), which can provide better and more complicated investigations of molecular systems. Furthermore, the wave function ($\phi(\vec{R},t)$) in quantum dynamics should be much more structured due to the nuclear motion. The nuclear motion can be evaluated in terms of a nuclear wave packet moving over the electronic potential surfaces in the system, where the nuclear wave packet can usually be chosen as a superposition of the eigenstates of the system.

One of the most simplest methods for solving the TDSE is the *standard method*. This method involves expanding the nuclear wave function (WF) ($\phi(\vec{R},t)$) into a product of a time-independent basis set for a chosen

electronic state (q) [37, 38]:

$$\begin{aligned}\phi^{(q)}(\vec{R},t) &= \phi^{(q)}(\vec{R}_1,\vec{R}_2,\cdots,\vec{R}_f,t)\\ &= \sum_{j_1=1}^{n_1}\cdots\sum_{j_f=1}^{n_f} C^{(q)}_{j_1\cdots j_f}(t)\chi^{(1)}_{j_1}(\vec{R}_1)\cdots\chi^{(f)}_{j_f}(\vec{R}_f)\\ &= \sum_{j_1\cdots j_f} C^{(q)}_{j_1\cdots j_f}(t)\prod_{k=1}^{f}\chi^{(k)}_{j_k}(\vec{R}_k).\end{aligned} \tag{1.6.2}$$

Here, f is the number of nuclear DOFs, n_k is the (nuclear) basis function for the kth ($k = 1, 2, ..., f$) DOF, and $\vec{R}_1, \cdots, \vec{R}_f$ are the nuclear coordinates. $\chi^{(k)}_{j_k}(\vec{R}_k)$ specifies the time-independent basis functions corresponding to the kth DOF, while $C^{(q)}_{j_1\cdots j_f}(t)$ are expansion coefficients that are dependent on time for the electronic state (q).

The Dirac-Frenkel variational principle (VP) can be used to derive equations of motion for the expansion coefficients $C_{j_1\cdots j_f}(t)$,

$$\langle\delta\phi(\vec{R},t)|\hat{H} - i\frac{\partial}{\partial t}|\phi(\vec{R},t)\rangle = \langle\delta\phi(\vec{R},t)|\hat{H}\phi(\vec{R},t) - i\dot{\phi}(\vec{R},t)\rangle = 0, \tag{1.6.3}$$

where the terms $\delta\phi$ and $\dot{\phi}$ are given by the following two equations [49]:

$$\delta\phi(\vec{R},t) = \sum_{l_1\ldots l_f}\frac{\partial\phi(\vec{R},t)}{\partial C_{l_1\ldots l_f}(t)}\delta C_{l_1\ldots l_f}(t) = \sum_{l_1\ldots l_f}\chi^{(1)}_{l_1}(\vec{R}_1)\cdots\chi^{(f)}_{l_f}(\vec{R}_f)\delta C_{l_1\ldots l_f}(t) \tag{1.6.4}$$

and

$$\dot{\phi}(\vec{R},t) = \sum_{j_1\cdots j_f}\dot{C}_{j_1\cdots j_f}(t)\chi^{(1)}_{j_1}(\vec{R}_1)\cdots\chi^{(f)}_{j_f}(\vec{R}_f). \tag{1.6.5}$$

By substituting the above two equations for eq. 1.6.3, the first-order differential equation with constant coefficients can be obtained

$$i\dot{C}_L(t) = \sum_J\langle\chi_L(\vec{R})|\hat{H}|\chi_J(\vec{R})\rangle C_J(t) = \sum_J\hat{H}_{LJ}C_J(t), \tag{1.6.6}$$

where $J = (j_1, \cdots, j_f)$ and $\chi_J(\vec{R}) = \prod_{k=1}^{f} \chi_{J_k}(\vec{R})$ for J, and similar notations for L are introduced. The matrix representation of the Hamiltonian can be given in the product basis set $\chi_{j_k}^{(k)}$: $\hat{H}_{LJ} = \langle \chi_{l_1}^{(1)} \cdots \chi_{l_f}^{(f)} | \hat{H} | \chi_{j_1}^{(1)} \cdots \chi_{j_f}^{(f)} \rangle$. With this method, the computational calculations are costly due to the dependence of the number of coupled equations on the number of DOFs f. For example, suppose we have five atoms and twenty basis functions selected per degree of freedom. The number of coupled equations equals $20^{(f)} = 20^9$, which makes it almost impossible to calculate such a huge equation ensemble with current computers. So, this approximation can allow us to deal with only three- or four-atom molecules, but we can still face difficulties in computational time and memory.

Therefore, we will move on to the next type of method, the so-called *time-dependent Hartree (TDH)* (also referred to as the time-dependent self-consistent field), which is more straightforward and cleverer than the standard method, to avoid the calculations of many coupled equations. In the TDH approach, the nuclear WF can be expressed as [49]:

$$\begin{aligned} \phi(\vec{R}_1, \vec{R}_2, \cdots, \vec{R}_f, t) &= a(t)\varphi_1(\vec{R}_1, t) \cdots \varphi_f(\vec{R}_f, t) \\ &= a(t) \prod_{k=1}^{f} \varphi_k(\vec{R}_k, t) = a(t)\Phi(t), \end{aligned} \tag{1.6.7}$$

where $a(t)$ is the time-dependent expansion coefficient that may include both real and complex parts, $\varphi_k(\vec{R}_k, t)$ are single-particle functions (SPFs) or orbitals for the kth degree of freedom of nuclei, and the terms $\varphi_1(\vec{R}_1, t) \cdots \varphi_f(\vec{R}_f, t)$, (or $\Phi(t)$) are called a Hartree product. Equation 1.6.7 may not determine the single-particle functions uniquely because phase and normalization factors might be shifted from one to another among SPFs. To gain unique equations of motion, one should introduce constraints that remove the non-uniqueness of the SPFs

$$i\langle \varphi_k(t) | \dot{\varphi}_k(t) \rangle = g_k(t), \tag{1.6.8}$$

where $g_k(t)$ is an arbitrary (but mostly real) function that we can choose according to the conditions. We can reach equations of motion by using VP as we did above for the standard method as follows (see ref. [37, 49] for more detail):

$$i\dot{\varphi}_k(t) = \left[\mathcal{H}^{(k)} - E + g_k(t)\right] \varphi_k(t) \tag{1.6.9}$$

$$i\dot{a(t)} = \left[E - \sum_{k=1}^{f} g_k(t)\right] a(t). \tag{1.6.10}$$

Here the eigenvalues E and Hamiltonian $\mathcal{H}^{(k)}$ can be specified by the forms:

$$E = \langle\Phi|\hat{H}|\Phi\rangle \tag{1.6.11}$$

and

$$\mathcal{H}^{(k)} = \langle\Phi^{(k)}|\hat{H}|\Phi^{(k)}\rangle. \tag{1.6.12}$$

Here, the eigenvalues (E) of the system can be time-dependent because the Hartree product Φ depends on time. Although many DOFs can be included in the calculations using this TDH method, they are not accurate enough due to restrictions imparted to the WF. In the next subsection, we will discuss the TDH by taking several configurations into account.

1.6.1 Multi-configuration time-dependent Hartree method

In this subsection, we will take a look at the multi-configuration time-dependent Hartree (MCTDH) [37–39, 49] method that combines standard, numerically exact wave function propagation and the time-dependent Hartree approximations. The MCTDH package [40] is extensively employed in many fields like scattering processes [50], photodissociation reactions [51, 52], and application of the complex absorbing potential (CAP) [53], absorp-

tion spectra calculations [54, 55]. Furthermore, in the MCTDH package, many types of programs are included to analyze the results of calculations obtained and compute observable quantities.

In the MCTDH approach, the nuclear WF can be considered a linear combination of Hartree products [37]:

$$\begin{aligned}\phi(\vec{R},t) &= \phi(\vec{R}_1,\cdots,\vec{R}_f,t)\\ &= \sum_{j_1=1}^{n_1}\cdots\sum_{j_f=1}^{n_f} A_{j_1\cdots j_f}(t)\varphi_1^{(1)}(\vec{R}_1,t)\cdots\varphi_f^{(f)}(\vec{R}_f,t)\\ &= \sum_{j_1=1}^{n_1}\cdots\sum_{j_f=1}^{n_f} A_{j_1\cdots j_f}(t)\prod_{k=1}^{f}\varphi_{j_k}^{(k)}(\vec{R}_k,t),\end{aligned} \tag{1.6.13}$$

where coefficients $A_{j_1\cdots j_f}(t)$ are the MCTDH expansion coefficients that are the time-dependent, and the $\varphi_{j_k}^{(k)}(\vec{R}_k,t)$ are the time-dependent single particle functions for the kth DOF. The SPFs can be expressed on a time-independent basis set:

$$\varphi_{j_k}^{(k)}(\vec{R}_k,t) = \sum_{i_1=1}^{N_k} c_{i_k}^{(k,j_k)}(t)\chi_{i_k}^{(k)}(\vec{R}_k), \tag{1.6.14}$$

where the $\chi_{i_k}^{(k)}(\vec{R}_k)$ are the primitive basis functions, in general, a discrete variable representation (DVR) or fast fourier transformation (FFT) function that depends on the nuclear coordinate $\vec{R}_k$. Because the MCTDH wave function representation (in eq. 1.6.13) is not unique (as in the case of the TDH approximation), but uniquely defined propagation can be obtained by introducing the constraints

$$\langle\varphi_i(t=0)|\varphi_j(t=0)\rangle = \delta_{ij} \tag{1.6.15}$$

and

$$\langle\varphi_i^{(k)}(t)|\dot{\varphi}_j^{(k)}(t)\rangle = -i\langle\varphi_i^{(k)}(t)|\hat{g}^{(k)}|\varphi_j^{(k)}(t)\rangle \tag{1.6.16}$$

on the single particle functions. Here, $\hat{g}^{(k)}$ is a constraint operator that might be a Hermitian or arbitrary operator acting on the kth DOF.

The Dirac-Frenkel variational principle (equation 1.6.3 used for the standard and TDH approximations) can also be used to describe equations of motion in the MCTDH method, where the varied $\phi^{'}$ and variation $\delta\phi$ wave functions take the following forms, respectively:

$$\begin{aligned}\phi^{'} &= \sum_{j_1}^{n_1}\cdots\sum_{j_f}^{n_f}(A_{j_1\cdots j_f}+\delta A_{j_1\cdots j_f})(\phi_{j_1}^{(1)}+\delta\phi_{j_1}^{(1)})\cdots(\phi_{j_f}^{(f)}+\delta\phi_{j_f}^{(f)}) \\ &= \sum_{j_1}^{n_1}\cdots\sum_{j_f}^{n_f}A_{j_1\cdots j_f}(\phi_{j_1}^{(1)}+\delta\phi_{j_1}^{(1)})\cdots(\phi_{j_f}^{(f)}+\delta\phi_{j_f}^{(f)})+ \\ &\quad \sum_{j_1}^{n_1}\cdots\sum_{j_f}^{n_f}\delta A_{j_1\cdots j_f}(\phi_{j_1}^{(1)}+\delta\phi_{j_1}^{(1)})\cdots(\phi_{j_f}^{(f)}+\delta\phi_{j_f}^{(f)})\end{aligned} \tag{1.6.17}$$

and

$$\delta\phi = \phi^{'}-\phi = \sum_{j_1}^{n_1}\cdots\sum_{j_f}^{n_f}A_{j_1\cdots j_f}\sum_{k}\delta\varphi_{j_k}^{(k)}\prod_{k'\neq k}\varphi_{j_{k'}}^{(k')}+\sum_{j_1}^{n_1}\cdots\sum_{j_f}^{n_f}\delta A_{j_1\cdots j_f}\prod_{k}\varphi_{j_k}^{(k)}. \tag{1.6.18}$$

Here, the $\Phi_J = \prod_k \varphi_{j_k}^{(k)}$ and $A_J = A_{j_1\cdots j_f}$ (in eq. 1.6.18) are notation as we did in the previous section. In equation 1.6.17 only up to first-order variations are considered for the sake of simplicity. As for the first-order

derivative $\dot{\phi}$ (in eq. 1.6.3), one takes the form

$$\begin{aligned}\dot{\phi} &= \sum_{j_1}^{n_1}\cdots\sum_{j_f}^{n_f}\dot{A}_{j_1\cdots j_f}\prod_k\varphi_{j_k}^{(k)} + \sum_{j_1}^{n_1}\cdots\sum_{j_f}^{n_f}A_{j_1\cdots j_f}\dot{\varphi}_{j_1}^{(1)}\varphi_{(j_2)}^{(2)}\cdots\varphi_{j_f}^{(f)} + \cdots \\ &+ \sum_{j_1}^{n_1}\cdots\sum_{j_f}^{n_f}A_{j_1\cdots j_f}\dot{\varphi}_{j_f}^{(f)}\varphi_{(j_1)}^{(1)}\cdots\varphi_{j_{f-1}}^{(f-1)} + \cdots \\ &= \sum_{j_1}^{n_1}\cdots\sum_{j_f}^{n_f}\dot{A}_{j_1\cdots j_f}\prod_k\varphi_{j_k}^{(k)} + \sum_k\sum_{j_1}\cdots\sum_{j_f}A_{j_1\cdots j_f}\dot{\varphi}_{j_k}^{(k)}\prod_{k'\neq k}\varphi_{j_{k'}}^{(k')}.\end{aligned} \tag{1.6.19}$$

After some notation and algebra, the MCTDH working coupled equations can be obtained as follows:

$$i\dot{A}_J = \sum_L\langle\Phi_J|\hat{H}|\Phi_L\rangle A_L - \sum_{k=1}^{f}\sum_{l=1}^{n_k}\hat{g}_{j_kl}^{(k)}A_{J_l^k} \tag{1.6.20}$$

and

$$i\dot{\varphi}^{(k)} = \hat{g}^{(k)}\mathbf{1}_{n_k}\varphi^{(k)} + (1-P^{(k)})\left[(\rho^{(k)})^{-1}\langle\hat{\mathbf{H}}\rangle^{(k)} - \hat{g}^{(k)}\mathbf{1}_{n_k}\right]\varphi^{(k)} \tag{1.6.21}$$

where $\mathbf{1}_{n_k}$ is the $n_k\times n_k$ unit matrix, the vector notation for the single-particle functions has been adopted as $\varphi^{(k)} = (\varphi_1^{(1)},\cdots,\varphi_{n_k}^{(k)})^T$, and $\langle\hat{\mathbf{H}}\rangle^{(k)}$ stands for the mean-field operator with respect to the single-hole functions. The density matrix $\rho^{(k)}$) can be adopted in the form

$$\begin{aligned}\rho_{jl}^{(k)} &= \langle\phi_j^{(k)}|\phi_l^{(k)}\rangle \\ &= \sum_{j_1}\cdots\sum_{j_{k-1}}\sum_{j_{k+1}}\cdots\sum_{j_f}A^*_{j_1\cdots j_{k-1}j_{k+1}\cdots j_f}A_{j_1\cdots j_{k-1}lj_{k+1}\cdots j_f} \\ &= \sum_J^K A^*_{J_j^k}A_{J_l^k}.\end{aligned} \tag{1.6.22}$$

The term $P^{(k)}$ (in eq. 1.6.21) is the projector introduced on the space spanned by the single-particle functions for the nuclear degree of freedom kth

$$P^{(k)} = \sum_{j=1}^{n_k} |\varphi_j^{(k)}\rangle\langle\varphi_j^{(k)}|, \tag{1.6.23}$$

and the notation for constraining $g_{j_k l}^{(k)}$ (in eq. 1.6.21) gets the form

$$g_{j_k l}^{(k)} = \langle\varphi_{j_k}^{(k)}|g^{(k)}|\varphi_l^{(k)}\rangle. \tag{1.6.24}$$

The choice of this operator $g^{(k)}$ is arbitrary that does not affect the quality of the MCTDH wave function. However, a reasonable choice of this operator can reduce the performance of calculations [37].

The MCTDH scheme is a very efficient and accurate wave packet propagation method developed by the Heidelberg group [38, 40]. It employs the DVR basis functions. With the DVR basis, both the potential and kinetic energy operators (using a FFT) can be simply evaluated as diagonal elements in matrix representation.

Chapter 2

Light-induced dissociation dynamics of the NaH molecule

Because NaH is a heteronuclear diatomic molecule, it has only one nuclear vibrational DOF in field-free space. Nevertheless, it has been known that the second DOF might be artificially created by applying an external field to the molecular system [26, 27, 56–61]. In such cases, the formation of light-induced CIs/ACs and their impacts on molecular dynamics can be investigated.

In this chapter, I investigate non-adiabatic molecular photodissociation dynamics by applying a classical EM field in the case of NaH (based on the work [62]). To understand the molecular dynamics of the sodium hydride molecule, the dissociation yields, the kinetic energy release spectra (KER) and the angular distributions of the dissociation fragments are computed employing pump and probe laser pulses. In addition, studying the influence of LICI and LIAC on the permanent dipole moments of NaH is another goal of this chapter.

This chapter is structured as follows: the first section 2.1 discusses the sodium hydride molecule and its working Hamiltonian, whereas the pump-

probe scheme and propagation of nuclear wave packet are presented in sections 2.2 and 2.3, respectively. The remaining two large sections are devoted to the results attained and the discussion parts of the work. At the end, a short conclusion for this chapter will be presented.

2.1 The NaH system and its Hamiltonian

The field-free Hamiltonian of a molecule can be computed using standard methods of quantum chemistry calculations, as discussed in section 1.2. Having obtained the relevant data, like the molecule's field-free potential energy surfaces, PDMs and TDMs, the subsequent step is to construct the working Hamiltonian by including these above-mentioned data and the external electric field. Because of the strong couplings between the electronic states in the presence of external electric fields with proper parameters, considerable changes can be observed in the molecular dynamics [17, 18, 63–70].

The three electronic states of NaH are considered in our numerical calculations, and they are labeled as $X^1\Sigma^+$ ($V_X(R)$), $A^1\Sigma^+$ ($V_A(R)$) and $B^1\Pi$ ($V_B(R)$) shown in Figure 2.1a, whereas panels (b) and (c) demonstrate the transition ($\vec{\mu}_{XA}$, $\vec{\mu}_{XB}$, $\vec{\mu}_{AB}$) and the permanent ($\vec{\mu}_X$, $\vec{\mu}_A$, $\vec{\mu}_B$) dipole moments of the system as a function of the internuclear distance (R). It is clear from panel (b) that the TDM between $V_X(R)$ and $V_A(R)$ states ($\vec{\mu}_{XA}$) is essential and effective in the region between R=6 and 9 au, whereas this region for the $\vec{\mu}_{AB}$ corresponds to less than R=8 au because of their large magnitudes. Also, as we will see in the next section, these regions correspond to the positions of LICIs and LIAC. The transition and permanent dipole moments can be defined by the forms

$$\hat{\vec{\mu}}_{ij}(R) = -\langle\psi_i^e|\sum_k r_k|\psi_j^e\rangle \tag{2.1.1}$$

$$\hat{\vec{\mu}}_i(R) = -\langle \psi_i^e | \sum_k r_k | \psi_i^e \rangle, \tag{2.1.2}$$

respectively, where ψ_i^e and ψ_j^e are the wave functions of the relevant electronic states (i,j=1,2,3).

Although the earlier works [71–73] have done simulations to gain the electronic structure calculations for the NaH system using the multiconfiguration self-consistent field, we decided to get the PESs, TDMs and PDMs quantities (for this project [62]) using one of the most accurate and productive ab initio calculations, the Molpro quantum package [35, 36]. The method that we have used is the multi-reference configuration interaction [42] at the level of the augmented correlation-consistent quintuple zeta (aug-cc-pV5Z). The molecule has the $C_{2\nu}$ symmetry point group, which has four irreducible representations: A_1, B_1, B_2 and A_2. The number of active electrons and molecular orbitals in each irreducible representation is equal to $A_1 \rightarrow 2/5$, $B_1 \rightarrow 0/2$, $B_2 \rightarrow 0/2$ and $A_2 \rightarrow 0/0$.

In our numerical simulations, the total Hamiltonian $\hat{H}_{tot}$ consists of the isolated molecular Hamiltonian ($\hat{H}_{mol}$) and the interaction ($\hat{H}_{inter}$) part with the pump and probe lasers; namely, $\hat{H}_{tot} = \hat{H}_{mol} + \hat{H}_{inter}$, as discussed in section 1.5. While the first term, $\hat{H}_{mol}$, contains the potential kinetic energies and permanent dipole moments of each electronic state, the interaction term $\hat{H}_{inter}$ expresses the scalar product of an external field and dipole moments: $\hat{H}_{inter} = -\vec{E}(t) \cdot \hat{\vec{\mu}}(R)$. In case the three singlet electronic states $V_X(R)$, $V_A(R)$ and $V_B(R)$ (in Fig. 2.1a) of NaH are taken into account, our total working Hamiltonian can have the three-by-three matrix

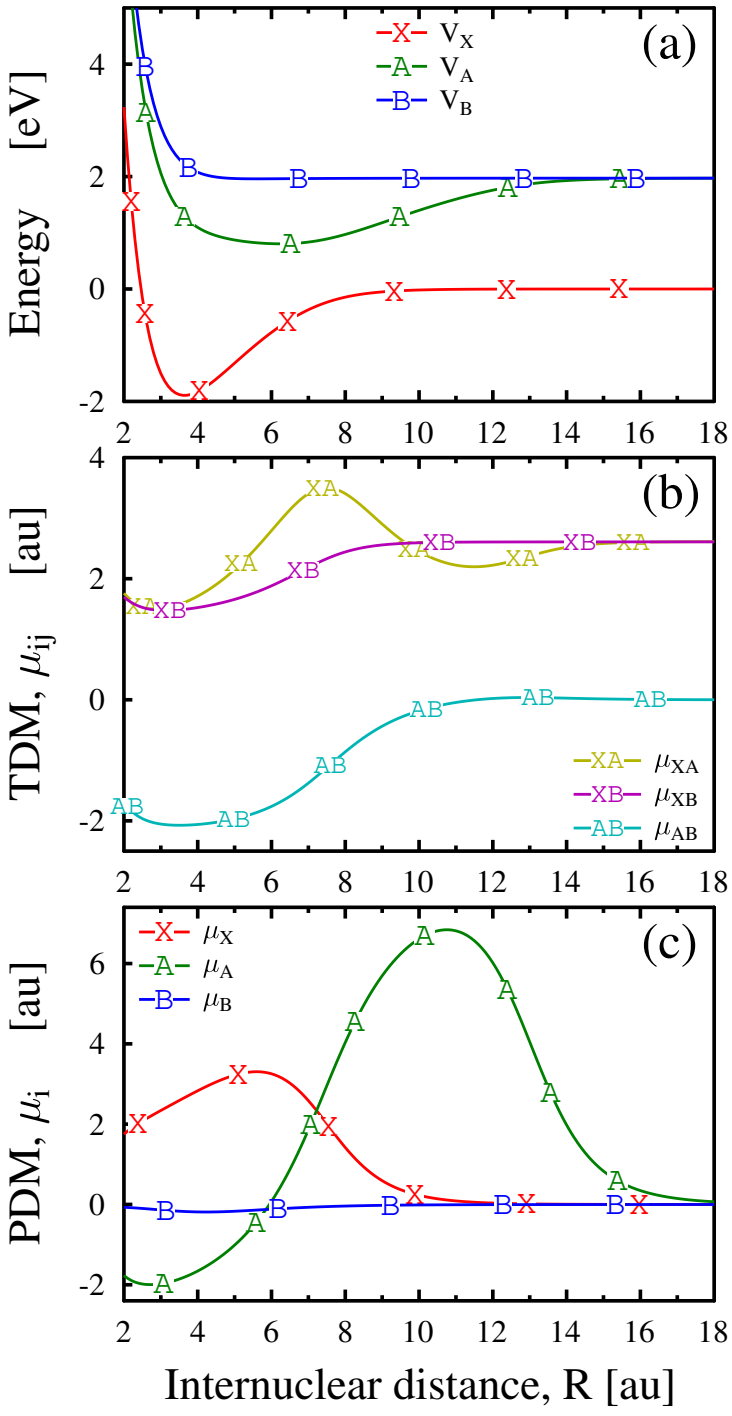

Figure 2.1: (a) Three lowest singlet adiabatic potential energy surfaces of the NaH molecule as a function of internuclear distance (R). (b) Panel shows transition dipole moments (μ_{ij}) between electronic states, while permanent dipole moments (μ_i) of each electronic state are visualized in panel (c).

form

$$\hat{H}_{tot} = \begin{pmatrix} \hat{T} + V_X(R) & 0 & 0 \\ 0 & \hat{T} + V_A(R) & 0 \\ 0 & 0 & \hat{T} + V_B(R) \end{pmatrix} +$$

$$- \vec{E}(t) \begin{pmatrix} \vec{\mu}_X(R)\cos(\theta) & \vec{\mu}_{XA}(R)\cos(\theta) & \vec{\mu}_{XB}(R)\sin(\theta) \\ \vec{\mu}_{AX}(R)\cos(\theta) & \vec{\mu}_A(R)\cos(\theta) & \vec{\mu}_{AB}(R)\sin(\theta) \\ \vec{\mu}_{BX}(R)\sin(\theta) & \vec{\mu}_{BA}(R)\sin(\theta) & \vec{\mu}_B(R)\cos(\theta) \end{pmatrix}, \quad (2.1.3)$$

where $\hat{T} = \hat{T}_{vib} + \hat{T}_{rot} = -\frac{1}{2M_r}\frac{\partial^2}{\partial R^2} + \frac{L^2_{\theta\phi}}{2M_r R^2}$ are the kinetic energy operators related to the vibrational and rotational motions in the molecule, respectively. R and (θ, ϕ) are the vibrational and rotational coordinates of the molecule, respectively. M_r is the reduced mass, and $L_{\theta\phi}$ is the angular momentum operator of the system, while the rotational coordinate, θ, expresses the angle between the internuclear axis of the system and the polarization direction of the applied laser field $\vec{E}(t)$ comprising pump and probe pulses. It needs to be noted that the each permanent dipole moment and the transition dipole moments between $V_X(R)$ and $V_A(R)$ states ($\vec{\mu}_{AX}$ or $\vec{\mu}_{XA}$) are parallel with the molecule's axis ($\cos(\theta)$ in eq. 2.1.3), while the transition dipole moments corresponding to the $\Sigma \leftrightarrow \Pi$ transitions ($\vec{\mu}_{XB}$ and $\vec{\mu}_{AB}$) possess a perpendicular direction with the molecular axis ($\sin(\theta)$). In addition, the rotational coordinate (θ) is considered a constant parameter in the 1D simulations, whereas it is set to the dynamical variable in the 2D simulations.

2.2 Description of the pump-probe scheme

Usually, when the molecule is exposed to the classic electromagnetic field, the interaction terms between the applied electric field and the molecule appear (see the second matrix of eq. 2.1.3). Throughout the whole computational simulation, the linearly polarized laser pulse (marked as $\vec{E}(t)$ in equation 2.1.3) has been chosen to investigate the molecular dissociation dynamics, comprising the sum of the pump and probe pulses:

$$\begin{aligned}\vec{E}(t) =& \vec{E}_{pm}(t) + \vec{E}_{pr}(t) = \\ & E_{pm_0} f_{pm}(t)\cos(\omega_{pm}t) + E_{pr_0} f_{pr}(t)\cos(\omega_{pr}t),\end{aligned} \tag{2.2.1}$$

where the term $\vec{E}_{pm}(t)$ stands for the pump pulse carrying energy ω_{pm} and amplitude E_{pm_0} to transfer the molecular dynamics of the system from the $V_X(R)$ state to the $V_A(R)$ state, while the probe pulse $\vec{E}_{pr}(t)$ carrying energy ω_{pr} and amplitude E_{pr_0} can transfer the subsequent population from $V_A(R)$ to the others, $V_X(R)$ and $V_B(R)$ states. The envelope functions $f_{pm}(t)$ and $f_{pr}(t)$ (in eq. 2.2.1), which possess cos-square-shaped pulses, take the following forms

$$\begin{aligned} f_{pm}(t) &= \Theta_{step}(t-T)\cos^2\left(\frac{\pi(t-t_{pm_0})}{\tau_{pm}}\right) \\ f_{pr}(t) &= \Theta_{step}(t-T)\cos^2\left(\frac{\pi(t-t_{pr_0})}{\tau_{pr}}\right), \end{aligned} \tag{2.2.2}$$

where $\Theta_{step}(t-T)$ is Heaviside's step function used to confine the laser waves to the desired position. For the time periods $t - T \geq 0$, Heaviside's step function switches on the field, while the field is switched off for times $t - T < 0$, where T is a parameter controlling the pulse duration.

Figure 2.2 gives a description of the pump-probe scheme applied to the three singlet electronic states of NaH. First, the pump pulse is used to transfer some amount of the population of $V_X(R)$ to $V_A(R)$ by $\hbar\omega_{pm}$, and

a crossing $LICI_{pump}$ (at around $R \approx 3.56$ au) between the shifted ground $[V_X(R) + \hbar\omega_{pm}]$ state and the excited $V_A(R)$ state is formed. In the second step, the probe pulse is applied with different delay times in order to make the $V_A(R)$ state couple with the remaining two states. The $V_A(R)$ state can be shifted upwards and downwards (the dotted green lies in figure 2.2a) by the probe energy $\hbar\omega_{pr}$ in the Floquet framework [26, 27, 65]. Two LICIs between the upward shifted first excited state $[V_A(R)+\hbar\omega_{pr}]$ and the second excited $V_B(R)$ state (see upper or lower $LICI_1$ and $LICI_2$ points at R $\approx$ 4.85 and 7.47 au, respectively in Fig. 2.2a), and one LIAC between the downward shifted first excited state $[V_A(R) - \hbar\omega_{pr}]$ and the ground $V_X(R)$ state (at R $\approx$ 7.8 au in Fig. 2.2a) are formed.

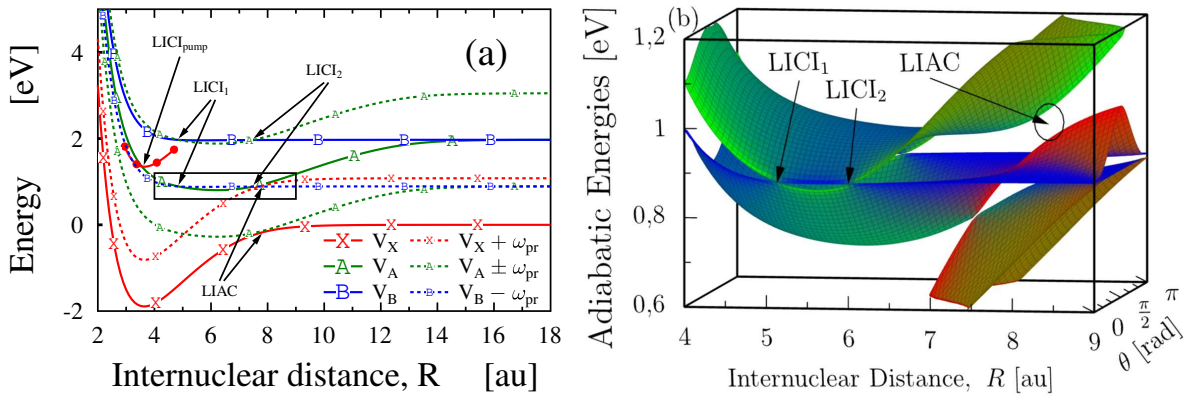

Figure 2.2: The pump-probe scheme. (a) The solid curves show the three singlet adiabatic potential energies in the field-free space. The relevant dashed curves demonstrate the field-dressed states due to the pump (ω_{pm}=3.24 eV) and probe (ω_{pr}=1.08 eV) laser pulses. The location of the LICIs ($LICI_{pump}$, $LICI_1$ and $LICI_2$) and LIAC are also indicated. (b) A cut of light-induced three adiabatic PESs computed for the probe pulse intensity ($I_{pr} = 1 \cdot 10^{12} W/cm^2$) is demonstrated. The coloring indicates the diabatic states that make up the different points of the adiabatic surfaces: red, $V_X(R)$; green, $V_A(R)$; and blue, $V_B(R)$

In the whole computational simulations, the pump and probe pulse durations are fixed as $\tau_{pm} = 8$ fs and $\tau_{pr} = 20$ fs, respectively. The starting points of the corresponding pulses are set to $t_{pm_0} = 0$ and $t_{pr_0} = 0...1000$ fs. The delay time is the difference between the centers of the two pulses. Because the pump and probe pulse durations and the starting time of the

pump pulse are fixed for all numerical simulations, the delay time depends only on the starting time of the probe pulse in our case ($t_{del} = t_{pr_0} + 6$). The energy of the pump needed to excite the system from the ground state into the first excited one in the vicinity of the Franck-Condon (FC) region is set to 3.24 eV, and the intensity and pulse duration of the pump are set to $1 \cdot 10^{13} W/cm^2$ and 8 femtoseconds (fs), respectively. These three parameters for the probe equal 1.08 eV, $1 \cdot 10^{12} W/cm^2$ and 20 femtoseconds, respectively.

Unlike natural CIs, LICIs can be manipulated using the parameters of the applied laser pulse. The laser frequency, for example, helps to modify the position of LICI in molecules, and the strength of the couplings between electronic states can be controlled by the intensity of the electric laser applied. Increasing the frequency shifts the CI to a smaller internuclear distance and lower energy state, whereas decreasing the frequency has the opposite tendency. Because only constant-frequency laser pulses have been used in this work, the position of none of the LICIs and LIACs and their energy values have changed during the whole dynamical process.

2.3 Wave packet dynamics and numerical quantities

Once the eigenvalue problem or the time-independent Schrödinger equation (discussed in the preceding subsection 1.2) has been solved, we can move on to deal with the nuclear dynamics of a molecular system by using our working Hamiltonian given in eq. 2.1.3. One of the most elaborate and efficient time-dependent methods to study molecular dynamics is the MCTDH approach [37–40]. During the calculations, the Fast fourier transformation-discrete variable representation (FFT-DVR) was used to describe the vibrational degree of freedom (DOF), where the number of grid points was set to N_R=512 with a range of R=2.0 to 50.0 au. For describing the rotational DOF, Legendre polynomials $(P_j(\cos\theta)_{j=0,1,2,3,\ldots,N_\theta})$ were employed in our simulations with N_θ=91. The number of single particle functions was selected as $n_R = n_\theta = 28$ for both vibrational and rotational DOFs. All calculations correctly converged with these applied parameters.

By using the solution of the MCTDH equations (1.6.13 and 1.6.14) along with single particle as well as primitive basis functions, the kinetic energy release $P_{ker}(E)$, the total dissociation probability P_{diss}, and the angular distributions $P_{Ang}(\theta_j)$ of the molecular dissociation fragments can be calculated [37]. The KER typically refers to the energy that is released while a molecule is in the process of dissociation, which can be evaluated in the form:

$$P_{ker}(E) = \int_0^\infty dt \int_0^\infty dt' \langle \phi(\vec{R},t)|W(R)|\phi(\vec{R},t')\rangle e^{-iE(t-t')}. \tag{2.3.1}$$

Here, -iW indicates the complex absorbing potential (CAP) employed for the grid of the vibrational degree of freedom, taking the form

$$-iW(R) = -i\eta|R - R_c|^b \Theta_{step}(\pm(R - R_{st})). \tag{2.3.2}$$

Here, the parameters R_{st}, η, and b indicate the starting point, strength, and the order of the CAP, respectively, while the $\Theta_{step}(\pm(R - R_{st}))$ denotes Heaviside's step function. Heaviside function switches on the CAP for the internuclear distances $R \geq R_{st}$ au. In our simulations, $W = 1.2 \times 10^{-5} \cdot (R - 40)^3$ parameters have been selected carefully for all three states, which are satisfied with convergence conditions (selecting carefully these parameters and other conditions are described in the ref. [40]). The angular distributions of molecular fragments can supply dissociation yields while the molecule is rotating, and its form can be defined by equation 2.3.3:

$$P_{Ang}(\theta_j) = \frac{1}{w_j} \int_0^\infty dt \langle \phi(\vec{R}, t) | W_{\theta_j} | \phi(\vec{R}, t) \rangle, \tag{2.3.3}$$

where the term $-iW_\theta$ is the projection of the CAP to a specific point of the angular grids ($j = 0, 1, \ldots, N_\theta$), and w_j is the weight related to these grid points in accordance with the used DVR. Another important physical quantity is the probability of the dissociation of a molecular system; it can be determined by eq. 2.3.4

$$P_{diss} = \int_0^\infty dt \langle \phi(\vec{R}, t) | W | \phi(\vec{R}, t) \rangle. \tag{2.3.4}$$

2.4 Light-induced dissociation

In this section, light-induced molecular dissociation of NaH is discussed with the help of the applied pump-probe scheme. Before discussing the dissociation dynamics of the system, it is important to examine the field-free vibrational motion of the wave packet on the initially populated $V_A(R)$ potential energy surface (see Fig. 2.3). The field-free nuclear wave packet

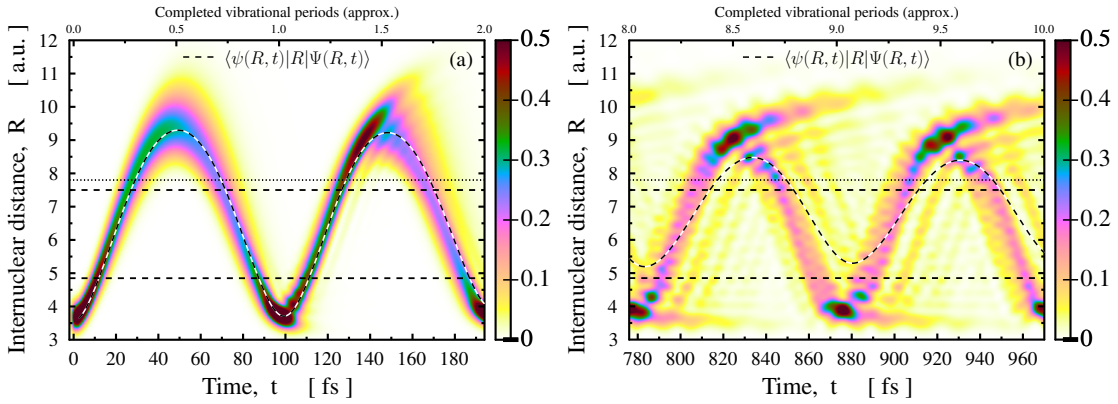

Figure 2.3: Field-free nuclear wave packet vibrational motion on the $V_A(R)$ state where propagation time $t = 0 - 196$ fs and 784-980 fs for panels (a) and (b), respectively. The color map shows the time-dependent density of the nuclear wave packet: the darker the color, the larger the nuclear density value. Besides, the time-dependent average of the internuclear distance, $\langle\psi(R,t)|R|\Psi(R,t)\rangle$, is also demonstrated with dashed line. For both panels, the horizontal dashed lines (at around $R \approx 4.85$ and $R \approx 7.5$ au) are the locations of the $LICI_1$ and $LICI_2$ between $V_A(R)$ and $V_B(R)$, whereas the horizontal dotted line (at around $R \approx 7.8$ au) is the location of the LIAC between $V_X(R)$ and $V_A(R)$.

motion on $V_A(R)$ as a function of propagation time is visualized in Fig. 2.3 when only the pump pulse has been applied. As the pump is utilized, about 51% of the ground state population is moved to the first excited state $V_A(R)$, whereas nearly 2.2% of the ground state population is transferred to the $V_B(R)$ state. The transferred nuclear wave packet on $V_A(R)$ moves periodically back and forth within an interval of $R \approx 3 - 11$ au. A cut for the nuclear density corresponding to the initial propagation time (for $t = 0 - 196$ fs) is relatively well-localized (see the color map in Fig. 2.3a), while the second time domain cut ($t = 784 - 980$ fs) is quite diffused (see

panel (b)). Another interesting and noticeable thing is that the $V_A(R)$ state nuclear wave packet motion intersects with the locations of the degeneracy points ($LICI_1$, $LICI_2$ and $LIAC$) at some points of propagation times (see Fig. 2.3). These crossing points of the wave packet can play a crucial role in dissociation yields. To explain this relation between dissociation yields and the positions of $LICI_1$, $LICI_2$ and $LIAC$ on the molecular dissociation, let's address Fig. 2.4.

In Fig.2.4, dissociation probabilities of each singlet electronic state as a function of the delay time in the range from 0 to 937 femtoseconds are calculated in 1D and 2D. It is evident that the $V_B(R)$ state is repulsive, while the $V_X(R)$ and $V_A(R)$ potentials support bound states (Fig. 2.1a). At

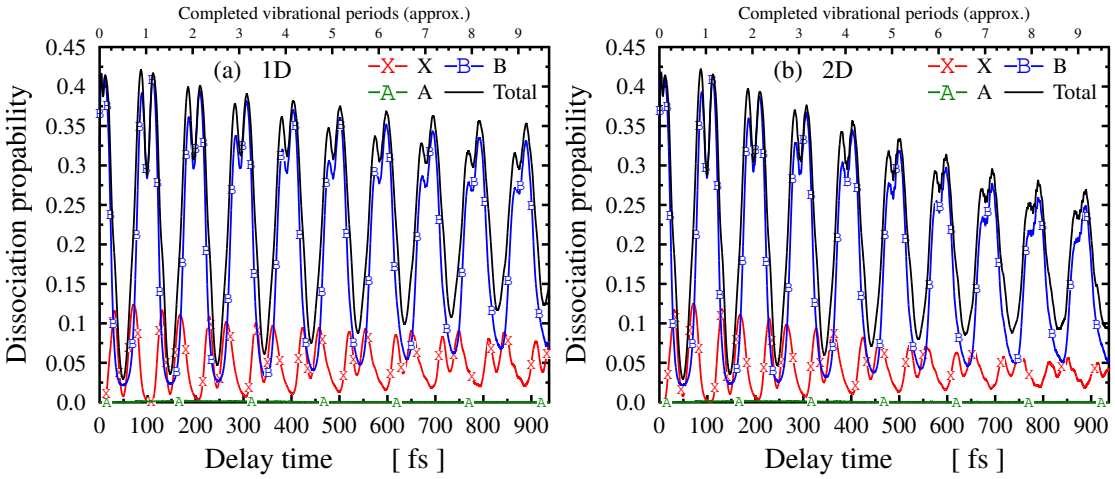

Figure 2.4: The red, green and blue curves denote the dissociation probabilities of the ground ($V_X(R)$), the first excited ($V_A(R)$), and the second excited ($V_B(R)$) states, respectively, while the black curve is the total dissociation probability of the NaH molecule. The range of the delay time is 0-937 fs on the X-axis. The comparisons of the probability of the dissociation in 1D and 2D are depicted in panels (a) and (b).

first sight, the dissociation probability mostly occurs on the second excited state (blue curve) in both 1D and 2D calculations, oscillating roughly from 2% to 42% during the whole delay time period, whereas similar oscillations are repeating in the case of the $V_X(R)$ state, with a range up to 12%. The $V_A(R)$ state dissociation yield (green line) is almost invisible on the scale used, and we will go back to this later when we discuss the influence of the

PDM on the dissociation.

The periodicity of the dissociation probability oscillations of $V_X(R)$ and $V_B(R)$ depends on the field-free nuclear wave packet vibrational motion on $V_A(R)$, which reaches the positions of the degeneracy points. As shown in Fig. 2.3, the field-free nuclear wave packet on the $V_A(R)$ state intersects with the positions of $LICI_1$, $LICI_2$ and $LIAC$ at particular propagation times. To illustrate, at t=15, 91, 114, 192... fs points, some amount of wave packet of $V_A(R)$ can pass to the $V_B(R)$ state through $LICI_1$ (see Fig. 2.3). As a result, when the delay time approaches these propagation times, the peaks of dissociation probability on the $V_B(R)$ state can be seen (see Fig. 2.4). The same holds for the case of $V_X(R)$, at t=30, 75, 130... fs points, some amount of wave packet of $V_A(R)$ can pass to the $V_X(R)$ state through LIAC. As a result, as the delay time approaches these propagation times, the peaks of dissociation probability on the $V_X(R)$ state can be observed (see Fig. 2.4). The position of $LICI_2$ between the two excited states does not have a strong effect (as compared with $LICI_1$) on the $V_B(R)$ state dissociation probability because of the value of μ_{AB} at $LICI_1$ and $LICI_2$: $\mu_{AB_{LICI_1}} \approx -2$ au at $R \approx 4.85$ au, and $\mu_{AB_{LICI_2}} \approx -1.1$ au at $R \approx 7.5$ au (see Fig. 2.1b).

Once only the pump is applied, nearly 2.2% of the population is dissociated on $V_B(R)$, but no dissociation occurs from $V_X(R)$. When the probe pulse is applied, as a next step, with various delay times, a large amount of the population of $V_A(R)$ is transferred to $V_B(R)$, while a smaller portion of the $V_A(R)$ population is transferred to $V_X(R)$. These populations are transferred through the LICIs and LIAC. Eventually, these transferred populations cause dissociation in the $V_X(R)$ and $V_B(R)$ states to some extent. Therefore, the main reason for the dissociation yields of the $V_X(R)$ and $V_B(R)$ states is related to the probe pulse effect.

It can be seen in Fig. 2.4 that the amplitude of the dissociation probabilities on $V_X(R)$ and $V_B(R)$ as a function of the delay time goes down monotonically, and this decrease is more noticeable in the 2D case (see Fig.

2.4b). Even though the maximum values of dissociation yields continuously go down, their minimum values continuously go up. This pattern can be interpreted as an effect of the increasing blurring of the nuclear wave packet with increasing delay time (t_{del}) values (see Fig. 2.3b). The difference in dissociation yields between 1D and 2D becomes noticeable from $t_{del} \approx 220$ fs and can reach up to 3.4% in $V_X(R)$ and 8% in $V_B(R)$. The variations between the 1D and 2D findings can be explained as a characteristic feature of the molecular rotation combined with the effects of the LICIs/LIAC and the various magnitudes/directions of the each TDM. During the pumping process, the axis of the molecular system rotates closer to the pump pulse polarization direction as time increases. A further population from $V_A(R)$ to $V_B(R)$ is transferred as the probe is applied. Less population from $V_A(R)$ to $V_B(R)$ can be transferred in the case of 2D since the the direction of μ_{AB} is perpendicular to the molecular axis. The less population to the $V_B(R)$, the less dissociation yield on this state.

The probe laser, on the other hand, couples the $V_A(R)$ and $V_X(R)$ states, and it supplies more efficient population transfer because μ_{XA} is parallel to the polarization direction of the probe pulse. As a result, Rabi oscillation starts between these two states, transferring some portions of the population back to the $V_A(R)$ state.

2.5 The flux analysis

Analyzing the flux results can help us understand detailed investigations and further descriptions of the system's dissociation dynamics. Therefore, in the following subsections, the fragment KER and angular distributions of each electronic state will be discussed to better interpret the results of the dissociation yields.

2.5.1 Kinetic energy release spectra

The system's photofragment kinetic energy release spectra of the can be calculated by using equation 2.3.1. The results for individual electronic states are given in Fig. 2.5 for the 1D and 2D frameworks, containing 12 panels from (a) to (l). We have chosen two delay time periods: shorter (t_{del} = 0-196 fs) and longer (t_{del} = 784-980 fs) time delays. It is obvious

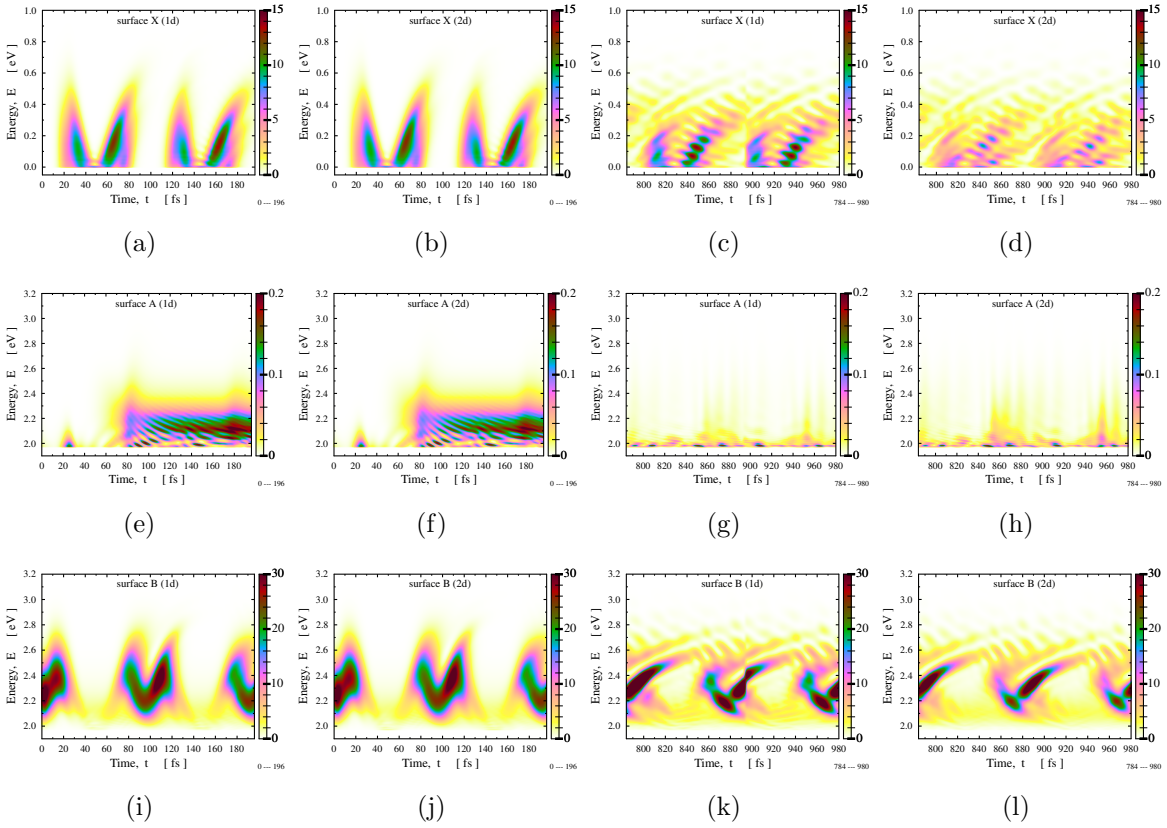

Figure 2.5: Color maps of KER of the photofragment of NaH as a function of delay time are depicted. Results obtained for individual channels are demonstrated in both 1D and 2D models. Panels (a)-(d) show the comparative results for the ground electronic state, while panels (e)-(h) and (i)-(l) show the same comparative results for the first and second excited states, respectively. The darker the color, the larger the value of the energy dissociated (the color scale is shown on the left-hand side of each panel).

that the 1D and 2D cases are almost identical for the shorter delay time periods for each electronic state (for example, panels (a) and (b) for the $V_X(R)$ state). It means that rotation initialized by the pump on surface

$V_A(R)$ has not yet achieved significant development for the shorter delay times prior to the probe pulse reaches the system. In other words, the system's rotation is not actively participating for this period. Unlike the shorter time delays, the discrepancy between the 1D and 2D models is already considerable for longer delay times. The 1D framework always supplies a more noticeable dissociation yield on the $V_X(R)$ and $V_B(R)$ states compared with the 2D case. Put differently, the molecular rotation is more significant as propagation time increases. The dissociation energy for the ground electronic state takes place around 0.2 eV (panels (a) to (d)), while the energy has been dissociated around 2-2.5 eV for the excited states (panels (e)-(l)).

2.5.2 The angular distributions

In this subsection, we discuss the dissociation yields of the system under two conditions: (i) θ is considered as a parameter (1D model); (ii) θ is considered as a variable, or the molecule is rotating between 0 and 180 degrees (2D model). In the 1D calculations, the kinetic energy related to the rotational motion ($\hat{T}_{rot} = \frac{L^2_{\theta\phi}}{2M_r R^2}$) is negligible in the calculations (so the molecule is frozen, with no rotation). In contrast, the term is included in the 2D calculations. Due to the symmetry of the angular distributions, the results are obtained from 0 to $\pi/2$ radians for all calculations. Figure 2.6 shows the phot-fragment angular distribution for the shorter and longer delay time periods in the 1D and 2D frameworks. As mentioned, the dissociation on $V_X(R)$ is only due to the transferred population from $V_A(R)$. The angle between the molecular axis and the polarization direction of the μ_{XA} is parallel ($\cos\theta$). Therefore, the dissociated population between the $V_X(R)$ and $V_A(R)$ states is zero at $\theta = \pi/2$ radians (panels (a) and (b)). For Figure 2.6b, the fragment angular distribution is much more spread out for

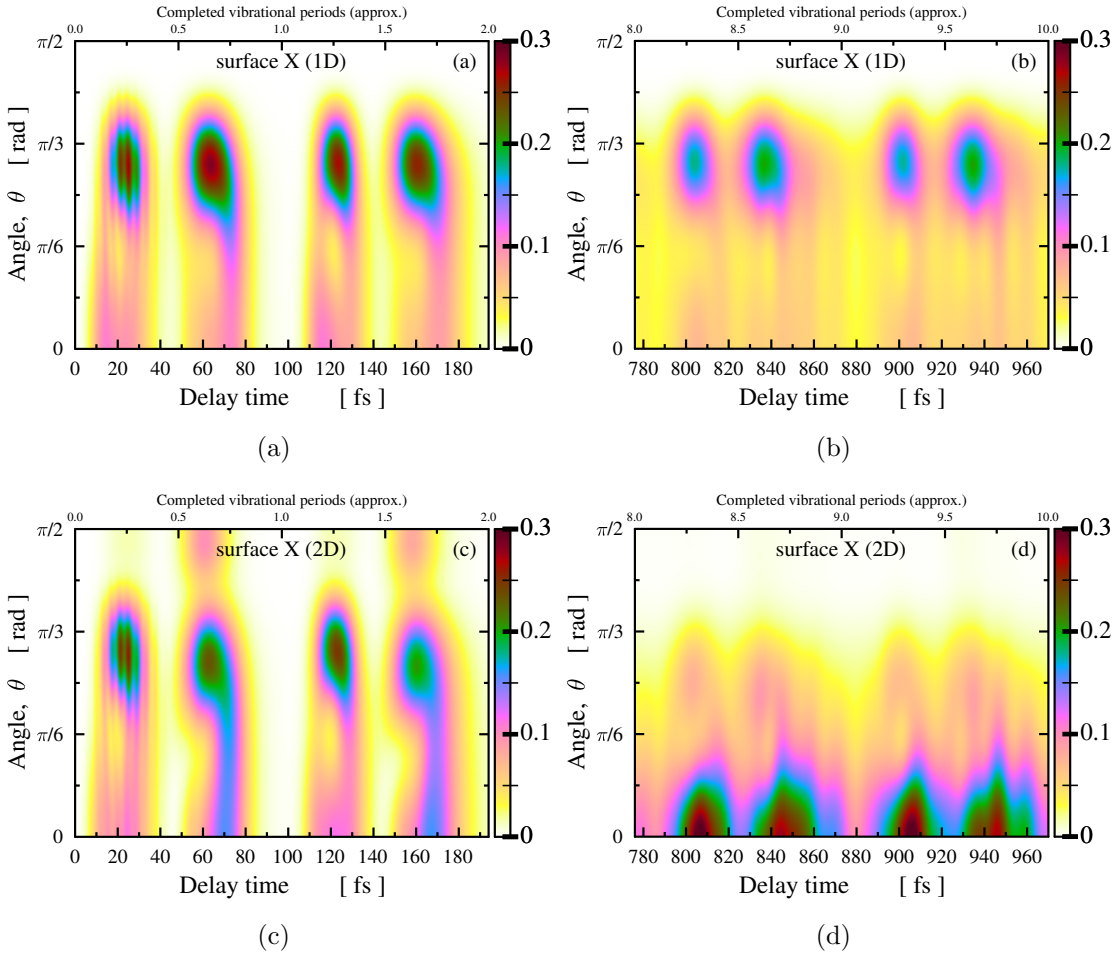

Figure 2.6: Photofragment angular distribution of the sodium hydride molecule for the $V_X(R)$ electronic state as a function of delay time. The obtained results are revealed for the shorter (panels (a), (c)) and longer delay time (panels (b), (d)) periods in the 1D and 2D frameworks.

the longer delay time period, which is associated with the diffuse nature of the field-free nuclear wave packet on $V_A(R)$ (see Fig. 2.3b). Nevertheless, the highest values of dissociation between the shorter and longer delay time periods remained in the same position. The results of the 2D calculations are demonstrated in Fig. 2.6c for the shorter delay times. The highest values of the angular distributions remain in the 2D cases at the same place as for the 1D cases, but the impact of the molecular rotation also appears. Unlike the 1D model for the short delay time, dissociation in the 2D case takes place at nearly $\theta = \pi/2$ radians, and more dissociation

happens at around t_{del} = 60 and 160 fs at θ = 0 radian in the 2D case owing to the effect of the rotation in the molecule. The former case can be interpreted by the fact that the probe can turn the molecular system towards $\theta = 0$ radians on the lower adiabatic surface and $\theta = \pi/2$ radians on the upper adiabatic surface. So, the probe rotates our system towards $\theta = 0$ or $\theta = \pi/2$ radians during the dissociation in the case of the shorter delay time period in 2D. For the longer delay time case (Fig. 2.6d), the landscape is totally different from the shorter case. The reason is associated with the influence of the pump pulse; namely, after applying the pump, the molecule has already had sufficient time to rotate toward the polarization direction of the pump. As a result, the large amount of dissociation yields can be collected at around $\theta = 0$ radians.

As for the dissociation yield on the $V_A(R)$ state demonstrated in Fig. 2.7, it is almost negligible in both 1D and 2D models due to the strong bound state (green curves in Figures 2.4a and 2.4b). Nevertheless, analyzing the structure of these panels is still worthwhile. The 1D and 2D results obtained are almost identical for the short delay times (panels (a) and (c)). In contrast, these results are totally different for the long delay times (panels (b) and (d)). The main noticeable difference between 1D and 2D for the long delay times is the increase in dissociation yield in the 2D scheme, particularly at around t_{del}=850 and 950 fs. The reasons might be interpreted as follows: (i) the pump pulse does not only transfer the populations from $V_X(R)$ to the other two states but also rotates the systems, and the molecule might rotate closer to the polarization direction of the pump pulse at longer delay times before the probe pulse is turned on; (ii) due to the influence of the presence of a two-photon process, the probe can also transfer back some amount of populations from the states $V_X(R)$ and $V_B(R)$ to the state $V_A(R)$.

The fragment angular distribution of the second excited electronic state is presented in Fig. 2.8. In the 1D model, it can be obliviously seen that dissociation yield does not occur either at θ= 0 or at $\theta = \pi/2$ radians

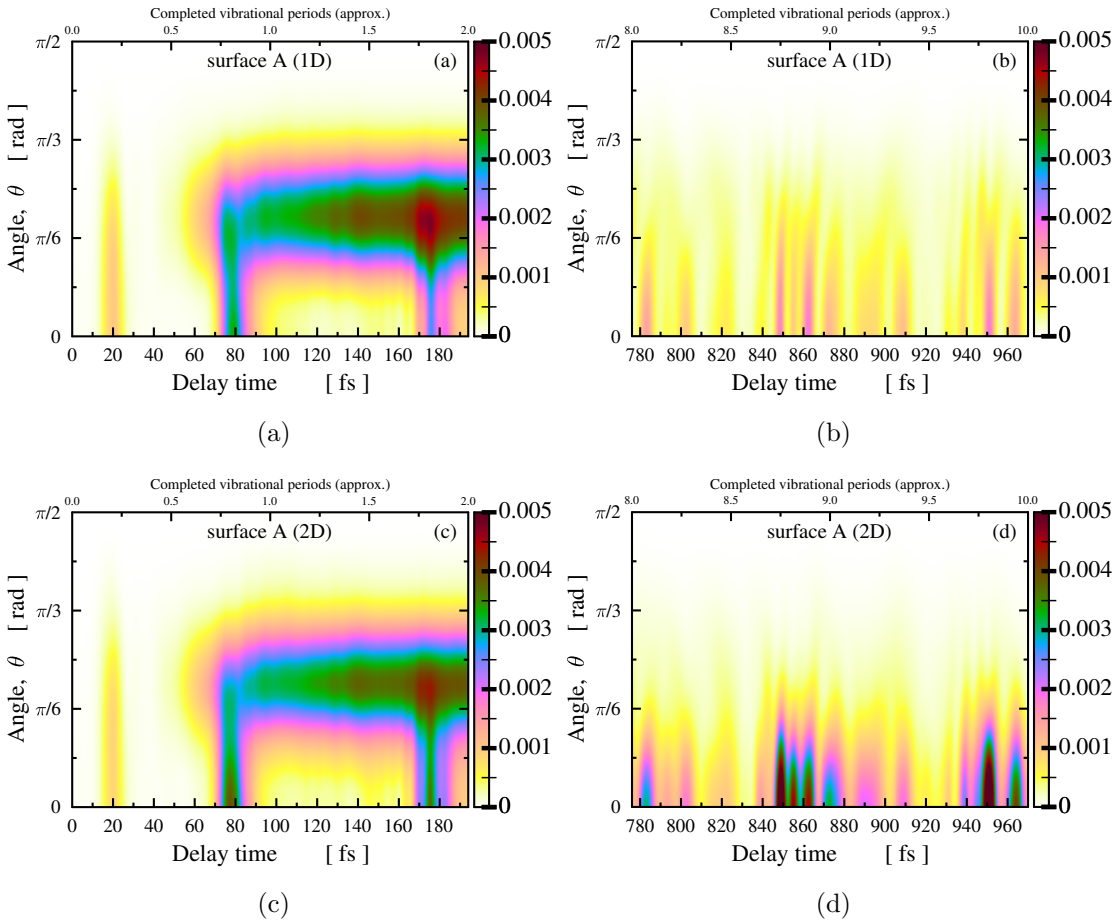

Figure 2.7: Photofragment angular distribution of the sodium hydride molecule for the $V_A(R)$ electronic state as a function of delay time. The obtained results are revealed for the shorter (panels (a), (c)) and longer delay time (panels (b), (d)) periods in the 1D and 2D frameworks.

(panels (a) and (b)). At $\theta = 0$ radians, there is no population transfer from either $V_X(R)$ or $V_A(R)$ to the state $V_B(R)$ due to the perpendicular angle between the polarization direction of the pump (as well as the probe) pulse and the molecule ($\sin\theta = 0$ at θ=0 degree). The reason for the lack of dissociation yield at $\theta = \pi/2$ radians can be explained as follows: because the pump pulse is not able to transfer any amount of population transfer from the $V_X(R)$ to $V_A(R)$ ($\cos\theta = 0$ at $\theta = \pi/2$), and hence the probe pulse cannot transfer further the population from the $V_A(R)$ to $V_B(R)$ states at this radian ($\theta = \pi/2$) at least when the system is frozen

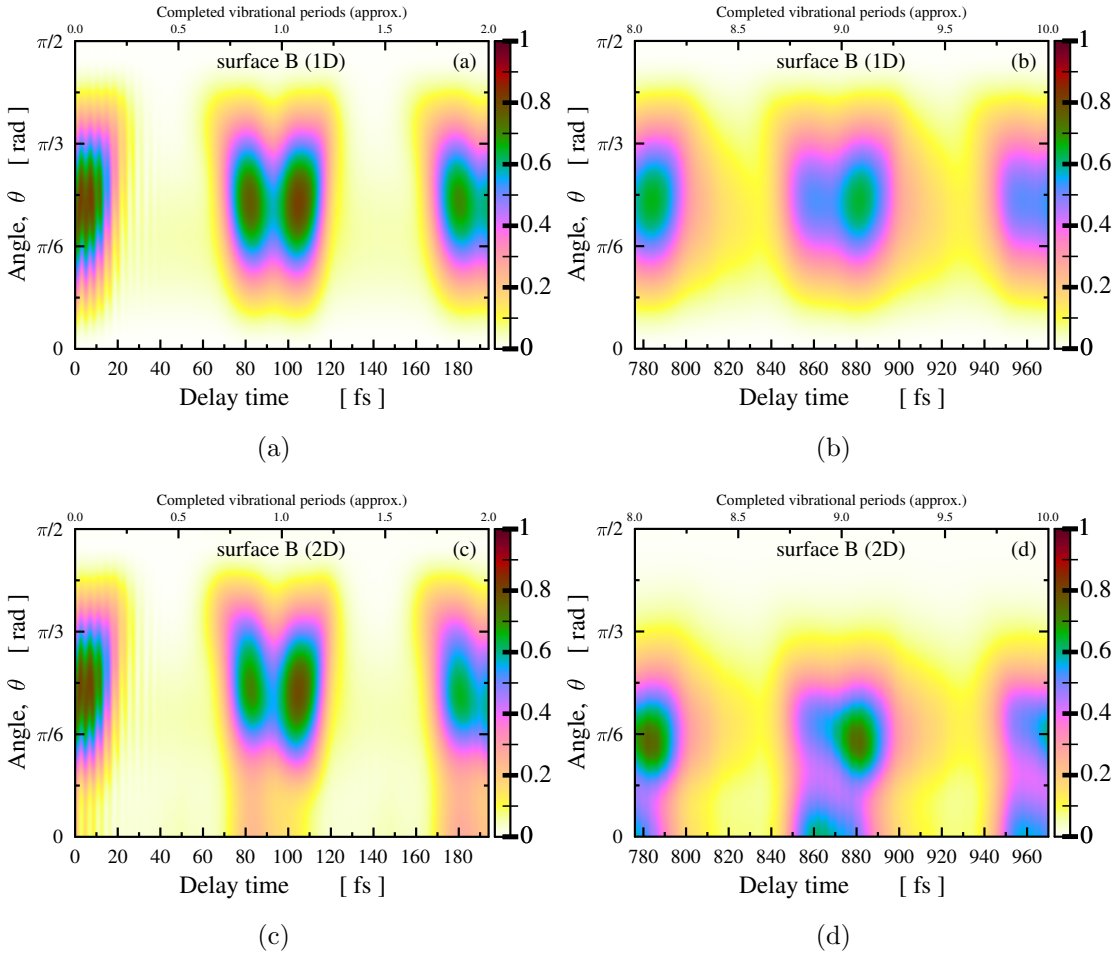

Figure 2.8: Photofragment angular distribution of the sodium hydride molecule for the $V_B(R)$ electronic state as a function of time delay. The obtained results are revealed for the shorter (panels (a), (c)) and longer delay time (panels (b), (d)) periods in the 1D and 2D frameworks.

(panels (a) and (b)). Conversely, at θ=0, dissociation on the $V_B(R)$ occurs in 2D and even becomes stronger in the long-time delay case (panel (d)). In 2D, the results can be interpreted as follows: when the pump is exploited, it builds up an anisotropic angular distribution of population in $V_A(R)$. Also, it evokes a rotational motion, which further amplifies this asymmetry as the delay time increases. More dissociated populations occur due to the probe effect that passes these populations from $V_A(R)$ to $V_B(R)$. The transferred molecules keep rotating further and further on $V_B(R)$ during the dissociation process and eventually are aligned parallel to the polarization

direction. The rotation effect becomes more and more important as the delay time increases further and the probe pulse detects molecules nearer to the polarization direction of the probe. Therefore, the larger values of the fragment angular distribution are shifted towards smaller θ angles, even at $\theta = 0$ radian (see Fig. 2.8c and 2.8d). As discussed in Fig. 2.6 and 2.7, the periodicity of the fragment angular distribution of the $V_B(R)$ state can again be explained as the result of the nature of the field-free vibrational motion of the nuclear wave packet on $V_A(R)$ (see Fig. 2.3).

2.6 The impact of the permanent dipole moment on dissociation

The NaH system has a large enough PDM owing to the heteronuclear molecule (see Fig. 2.1c). Some theoretical works[69, 72, 74] studied the NaH system where the PDMs were not included in their simulations. In this section, we will discuss the effect of PDMs on the molecular photodissociation yields and fragment angular distribution by including and excluding the PDMs of the system and compare the results obtained for the 1D and 2D frameworks. Fig. 2.9 shows the dissociation yields for all individual states with and without the permanent dipole moment in 1D and 2D. It is evident from panel (a) that there is no effect of the PDMs of NaH on the dissociation probability of the $V_X(R)$ state because dissociation yields of the $V_X(R)$ state with and without PDMs in 1D are almost identical and the same holds for 2D. As for the second excited state (Fig. 2.9b), minor differences between with and without PDM can be seen in both 1D and 2D results. The 'no PDM' case has higher dissociation yields (compared to that including PDM) for 1D as well as for 2D. On the other hand, the role of the permanent dipole moment on the dissociation is significant for

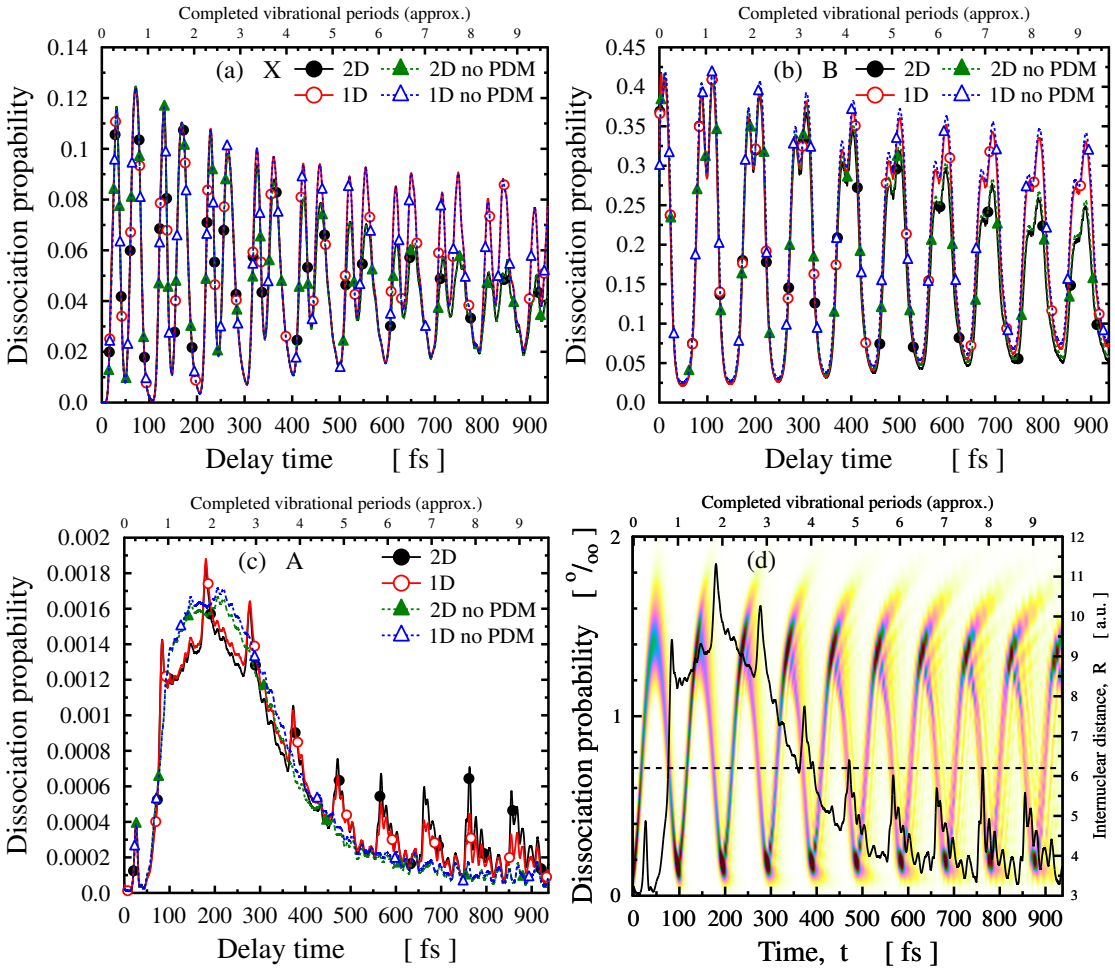

Figure 2.9: Dissociation yields for each individual state as a function of the delay time are shown between the pump and probe pulses. Panels (a) to (c) compare the dissociation probabilities in the 1D and 2D models by neglecting the PDMs ('no PDM' case in the title of the curves) for the ground, the first excited and the second excited states, respectively. Panel (d) shows the results for the 2D dissociation yield of the state $V_A(R)$ with PDM (scaled on the left side with percent) and the field-free nuclear wave packet motion (scaled on the right side with atomic units).

the $V_A(R)$ state (see panel (c)). The form of the 'with PDM' case displays a relatively complicated arrangement. It exhibits several consistent spike-shaped peaks, contrasting with the straightforward pattern of dissociation yield when the PDM is not used. Further numerical simulations have indicated that the background curve for the dissociation probability depends on the population that is passed from the dissociation region of surface $V_B(R)$ to surface $V_A(R)$ back with the help of the probe laser. Nevertheless, the decrease in the $V_A(R)$ dissociation, starting at $t_{del} \approx 220$ fs, results from an artificial effect caused by the nuclear wave packet absorption in the CAP region at the end of the grid. Upon further analysis of the results, it becomes evident that the peaks manifest when the nuclear wave packet returns from the right-hand side of the $V_A(R)$ state to the minima of the potential energy surface (see Fig. 2.9d). To enhance our understanding of the dissociation process occurring on the $V_A(R)$ surface, we conducted various simulations by artificially changing the values of PDMs and TDMs. Initially, we established the PDM value as $\mu_A = 2.5$ au. In this scenario, the peaks do not manifest, and the resulting outcome is nearly identical to the curve computed with $\mu_A = 0$ au ('no PDM' case in Fig. 2.9c). The magnitude of the spikes, on the other hand, is significantly affected by the slope of the μ_A function. If the permanent dipole function has a steeper slope, the peaks of the spikes are higher, whereas if the function is less steep, the peaks of the spikes become lower.

In Fig. 2.10, the fragment angular distribution for the $V_A(R)$ state is demonstrated with and without PDM in the 2D model. It is clear in all panels that there is no dissociated population at $\theta = \pi/2$ radians due to the parallel angle between the μ_{XA} and molecular axis. However, in the vicinity of θ=0 radian, it should be noted that the dissociation probability significantly increases, which can be seen as the direct consequence of the joint impact of the rotation as well as LICIs/LIAC. The impact of the rotation becomes more efficient owing to the influence of the PDM (see panels (c) and (d)). Also, since a substantial two-photon effect can be caused by

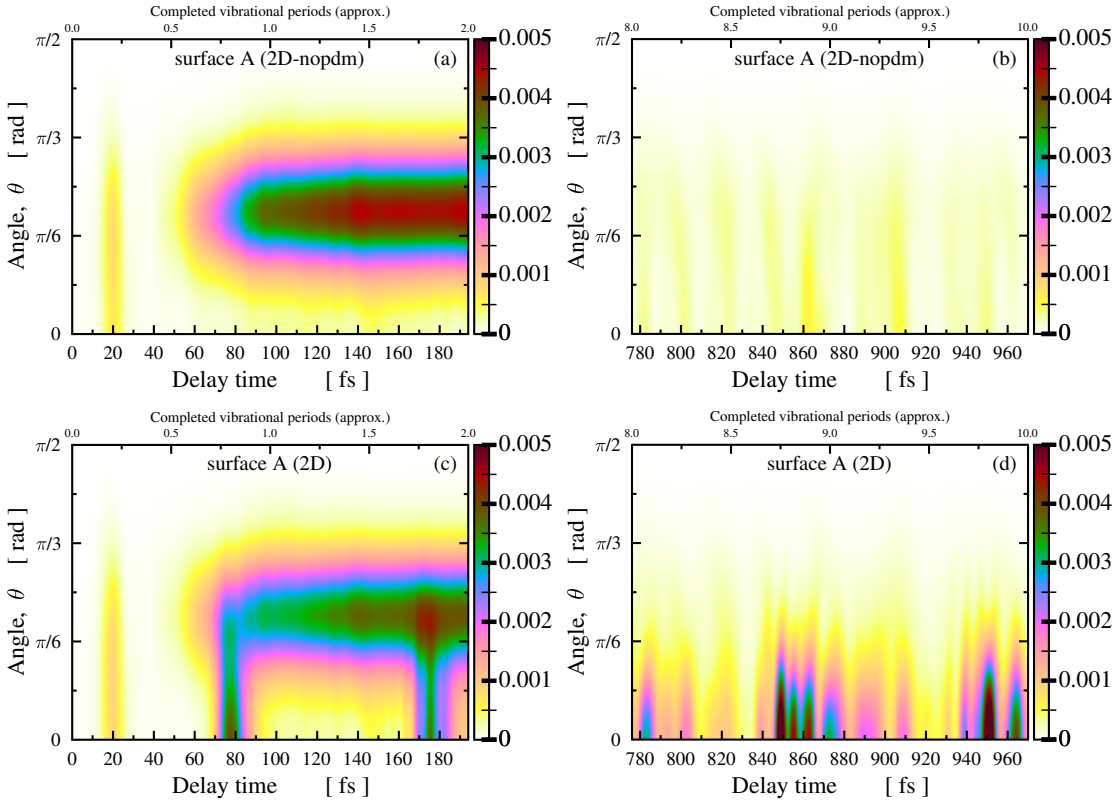

Figure 2.10: Photofragment angular distribution of the sodium hydride system for the first excited electronic state. The obtained results are manifested for the 2D scheme by neglecting (panels (a) and (b)) and including (panels (c) and (d)) the permanent dipole moments.

the probe pulse, a greater amount of population could revert with adequate kinetic energy from the $V_X(R)$ and $V_B(R)$ states to the $V_A(R)$ state, thereby augmenting the dissociation process. The spikes appearing around $\theta = 0$ radians at short delay times are also attributed to the existence of PDM. These spikes become more pronounced at longer delay times as a result of the heightened kinetic energy accumulated from the rotation.

2.7 Conclusions

The effect of the light-induced non-adiabatic phenomenon and the molecular rotational motion on the molecular dissociation dynamics have been studied for the NaH system involving the three singlet electronic states. All computational calculations are performed using the pump and probe pulses in 1D and 2D.

The influence of molecular rotational motion, LICIs/LIAC, and different magnitudes/directions of the system's TDMs resulted in discrepancies in the dissociation yields between the 1D and 2D calculations.

The dissociation yields of the system have been also investigated with the help of the data attained from the KER and the angular distribution of the photo fragments in the 1D and 2D cases.

The acquired findings clearly showed that the permanent dipole moments of the molecule did not play a significant role in the total dissociation probability, at least for the laser parameters that we applied. The impact of PDM on the dissociation yields of the $V_X(R)$ and $V_B(R)$ states is practically negligible.

Nevertheless, a rich pattern of the dissociation probability on the $V_A(R)$ curve was observed when the permanent dipole moment of the $V_A(R)$ state was included in the calculations. The structure of the curve itself originated from the back-transferred population to the $V_A(R)$ state. However, the fundamental physical mechanism responsible for the emergence of these peaks remains unclear. To this end, further investigations will be conducted by altering the external field's parameters.

Chapter 3

Topological aspects of cavity-induced degeneracies

In this chapter, a general overview of the topological aspects of cavity-induced degeneracy and the effect of LICI on the geometric phase will be discussed. Both natural and light induced CIs play a significant role in non-adiabatic processes as they serve as an efficient funnel to transfer energy from an upper adiabatic surface to a lower one. The presence of LICI can be determined by checking the valuedness of the wave function. The confined photonic mode couples the electronic states of the molecule, causing a strong mixing between these electronic states. As a result, mixed polaritonic states having both photonic and excitonic features appear in a molecular system. These polaritonic states arising from light-matter interaction can change the various dynamical, spectroscopic and other features of the molecules [13, 19, 21, 33, 34]. This was first highlighted by Herzberg and H.C. Longuet-Higgins [75, 76] that a real field-free adiabatic electronic state has a double value (plus and minus signs) around the degeneracy (LICI) points. Mead and Truhlar [77] introduced the effect of the geometric phase into a single electronic state problem, and later, Berry generalized

the "Berry phase" theory [78]. The total electron-nuclear wave function (WF) must be single-valued. Therefore, to maintain the single-valued nature of the total wave function, it is necessary to introduce a phase factor to the electronic wave function in the adiabatic representation. This phase factor ensures that the total wave function is single-valued.

In the first section of the chapter, the polyatomic formaldehyde (H_2CO) system will be the focus of discussion. The results (based on the work [8]) obtained for the non-adiabatic coupling terms between the adiabatic electronic states of the system and the Berry phase will be presented in sequential order. At the end, a short conclusion will be given.

3.1 The H_2CO system

The H_2CO, being a polyatomic molecule, has been selected for two major reasons: the first one is that the molecule lacks the natural LICI in the area that is close to the Franck-Condon region, and the second cause is that there are not any first-order non-adiabatic couplings between the ground and first singlet excited states near its equilibrium configuration. The planar equilibrium structure of the formaldehyde molecule with $C_{2\nu}$ symmetry in its ground electronic state ($V_X(R)$) and its normal modes are depicted in Figure 3.1. The $V_A(R)$ state holds a double-well structure along the ν_4 mode.

The time-independent problem has been solved at the level of CAM-B3LYP/6-31G* by making displacements along the two active normal modes, ν_2 (C=O stretch) and ν_4 (out-of-plane bend), while the other four modes (ν_1, ν_4, ν_5 and ν_6) have been made inactive (see panel (A) in Fig. 3.1). The values of PESs and TDMs have been interpolated with the help of the GLS package [79]. The only non-zero component of the TDM in the y-direction (with B_1 symmetry) exists, and the angle between the PDM and

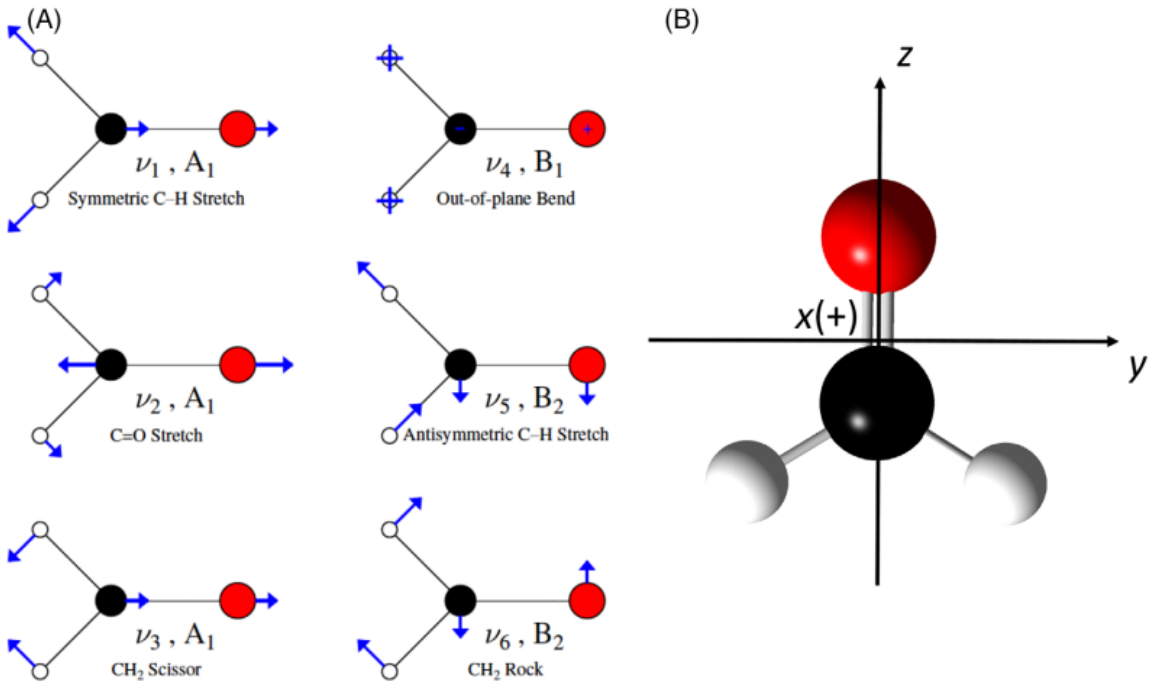

Figure 3.1: Various normal modes with $C_{2\nu}$ symmetry labels (panel A) and equilibrium structure (panel B) of the H_2CO molecule in its ground electronic state are demonstrated. Panel B illustrates the description of the body-fixed coordinate system, with the x-axis oriented outward, as denoted by the + sign.

TDM directions is perpendicular to each other. Having obtained electronic structure calculations, the time-dependent problem can be solved, in which the total molecule-cavity Hamiltonian ($\hat{H}_{tot}$) takes three components: the isolated molecule ($\hat{H}_{mol}$), cavity ($\hat{H}_{cav}$) and the molecule-cavity interaction ($\hat{H}_{int}$) Hamiltonians

$$\hat{H}_{tot} = \hat{H}_{mol} + \hat{H}_{cav} + \hat{H}_{int} = \hat{H}_{mol} + \hbar\omega_c \hat{a}^\dagger \hat{a} - g\hat{\vec{\mu}}\vec{e}(\hat{a}^\dagger + \hat{a}). \qquad (3.1.1)$$

Here $\hat{H}_{mol}$ contains the PESs ($V_X(R)$ and $V_A(R)$) and the kinetic energy related to the vibrational motion, $\hat{T}_{vib} = -\frac{1}{2M_r}\frac{\partial^2}{\partial R^2}$ where M_r is the reduced mass. $\hat{a}^\dagger$ and $\hat{a}$ are the creation and annihilation operators, while ω_c, g and $\vec{e}$ stand for cavity frequency, coupling strength and the polarization vector of the cavity mode, respectively. $\hat{\vec{\mu}}$ is the molecule's electric dipole moment operator. If two singlet electronic states S_0 (X^1A_1) and S_1 (A^1A_2) of H_2CO

are considered, the matrix representation of the diabatic Hamiltonian, $\hat{H}$, in the direct product basis of the two electronic states and Fock states $|n>$ (n=0,1,2,...) is given by the following form [80]:

$$\hat{H} = \begin{bmatrix} \hat{T}+V_X & 0 & W_1^X & W_1^{XA} & 0 & 0 & ... \\ 0 & \hat{T}+V_A & W_1^{XA} & W_1^A & 0 & 0 & ... \\ W_1^X & W_1^{XA} & \hat{T}+V_X+\hbar\omega_c & 0 & W_2^X & W_2^{XA} & ... \\ W_1^{XA} & W_1^A & 0 & \hat{T}+V_A+\hbar\omega_c & W_2^{XA} & W_2^A & ... \\ 0 & 0 & W_2^X & W_2^{XA} & \hat{T}+V_X+2\hbar\omega_c & 0 & ... \\ 0 & 0 & W_2^{XA} & W_2^X & 0 & \hat{T}+V_A+2\hbar\omega_c & ... \\ \vdots & \vdots & \vdots & \vdots & \vdots & \vdots & \ddots \end{bmatrix} \tag{3.1.2}$$

where $\hat{T}$ the kinetic energy operators including vibrational motion. $W_n^{XA} = -g\sqrt{n}\vec{\mu}_{XA}\vec{e}$, $W_n^X = -g\sqrt{n}\vec{\mu}_X\vec{e}$ and $W_n^A = -g\sqrt{n}\vec{\mu}_A\vec{e}$ are coupling terms between molecule and cavity interaction, where $\vec{\mu}_{XA}$ and $\vec{\mu}_X/\vec{\mu}_A$ are the transition dipole moment and permanent dipole moments, respectively. The polaritonic (or adiabatic) potential energy curves can be taken as the eigenvalues of the potential energy component (namely, $\hat{H}-\hat{T}I$, where I represents the identity matrix of appropriate dimension) of the Hamiltonian given in Equation (3.1.2) for each nuclear configuration. Representing the working Hamiltonian in the adiabatic picture is quite beneficial in most cases because the coupling matrix elements between different electronic states take place through only the nuclear kinetic energy terms (these couplings are zero through potential energies, as discussed in section 1.3). For two electronic states, adiabatic Hamiltonian can be obtained by diagonalizing the diabatic 2×2 matrix elements of $\hat{H}$ (in eq. 3.1.2)

$$\begin{bmatrix} V_A(R) & W_1^{XA} \\ W_1^{XA} & V_X(R)+\hbar\omega_c \end{bmatrix}. \tag{3.1.3}$$

This matrix pertains to the so-called singly-excited subspace having zero photon in the excited electronic state and one photon ($\hbar\omega_c$) in the ground electronic state. This singly-excited subspace gives rise to two adiabatic or polaritonic states in our system. These two polaritonic PESs can cross each other and form LICI whenever the two conditions $Q_4 = 0$ and $V_X(R)(Q_2^{CI}; Q_4 =$

$0) = V_A(R)(Q_2^{CI}; Q_4 = 0) - \hbar\omega_c$ are simultaneously fulfilled (see Figure 3.3). Here, Q_2 and Q_4 represent the active vibrational modes ν_2 (C=O stretch) and ν_4 (out-of-plane bend), respectively (see Fig. 3.1). The vibrational mode ν_2 (A_1 symmetry) serves as the tuning mode, while ν_4 is the coupling mode.

3.2 Results and discussions

In Fig. 3.2, the second and third lowest polaritonic curves as a function of normal coordinates (Q_2 and Q_4) of H_2CO coupled to a single cavity mode are demonstrated. The cavity frequency and coupling strength values are equal to $\omega_c = 29\ 000\ \text{cm}^{-1}$ and $g = 5.34 \times 10^{-2}$ au, respectively. The

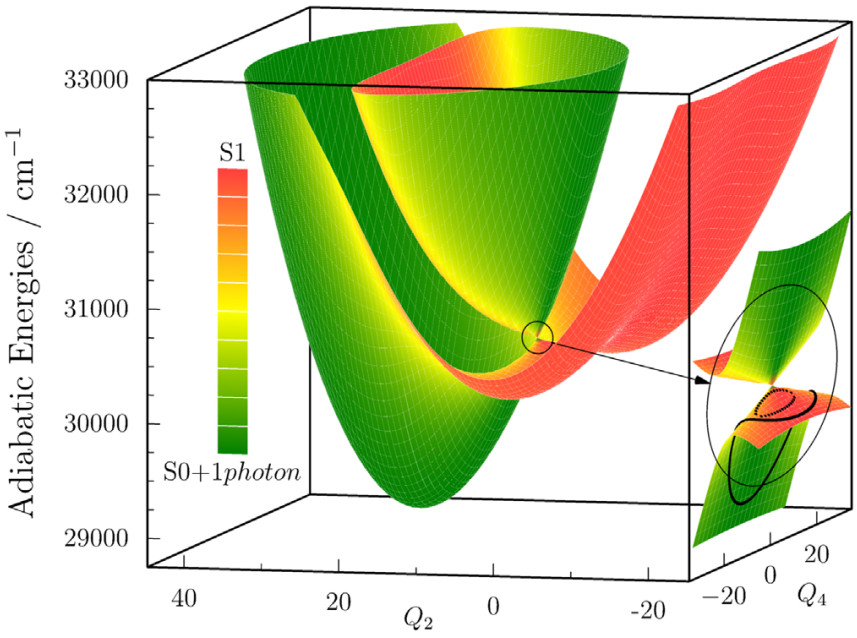

Figure 3.2: Two (upper and lower) polaritonic surfaces as a function of normal coordinates (Q_2 and Q_4) of the H_2CO system coupled to a single cavity mode are demonstrated. The frequency and coupling strength of the cavity are set to $\omega_c = 29\ 000\ \text{cm}^{-1}$ and $g = 5.34 \times 10^{-2}$ au, respectively. In the inset, the area of the cavity-induced conical intersection between these two polaritonic surfaces is depicted. Additionally, the inset shows two black curves illustrating various closed paths used in the topological phase calculations. The characteristics of the polaritonic potential energy surfaces (PoPESs) is represented by various colors, with the legend provided on the left, where the labels S_0 and S_1 denote the ground and excited electronic states of the molecule.

polaritonic light-induced conical intersection between the second and third polaritonic surfaces is depicted in the inset. The character of the polaritonic potential energy surfaces (PoPESs) is indicated by various colors, with the legend provided on the left, where the labels S_0 and S_1 denote the ground and excited electronic states of the molecule.

The two subsequent subsections are devoted to investigating the non-adiabatic coupling terms and the Berry phase when LICI is formed.

3.2.1 The non-adiabatic coupling terms

Non-adiabatic coupling terms can have a large magnitude near degeneracy between potential energy surfaces, making them pivotal in studying non-adiabatic phenomena in molecules. The NACTs (τ_{23Q_2} and τ_{23Q_4}) between the second and third (lower and upper) polaritonic states can be calculated as the derivatives of Φ with respect to the relevant nuclear degrees of freedom (Q_2, Q_4) [4]:

$$\begin{aligned} \tau_{23Q_2} &= \frac{\partial \Phi}{\partial Q_2} \\ \tau_{23Q_4} &= \frac{\partial \Phi}{\partial Q_4}, \end{aligned} \tag{3.2.1}$$

where Φ is the transformation angle of the ADT matrix. Fig. 3.3a shows the NAC terms (τ_{23Q_2} and τ_{23Q_4}) between 2nd and 3rd electronic states, whereas panel (b) displays the absolute value of the NAC vector, $|\tau_{23}| = \sqrt{\tau_{23Q_2}^2 + \tau_{23Q_2}^2}$ around the LICI. The used frequency of coupling strength of the cavity are equal to $\omega_c = 29,000\,\mathrm{cm}^{-1}$ and $g = 5.34 \times 10^{-2}$ au, respectively. It is clear that the NAC terms (panel (a)) are extremely large around the LICI point ($Q_2 \approx 4.8$ and $Q_4 = 0$). We can see the same fingerprint in the calculations of their absolute value shown in panel (b).

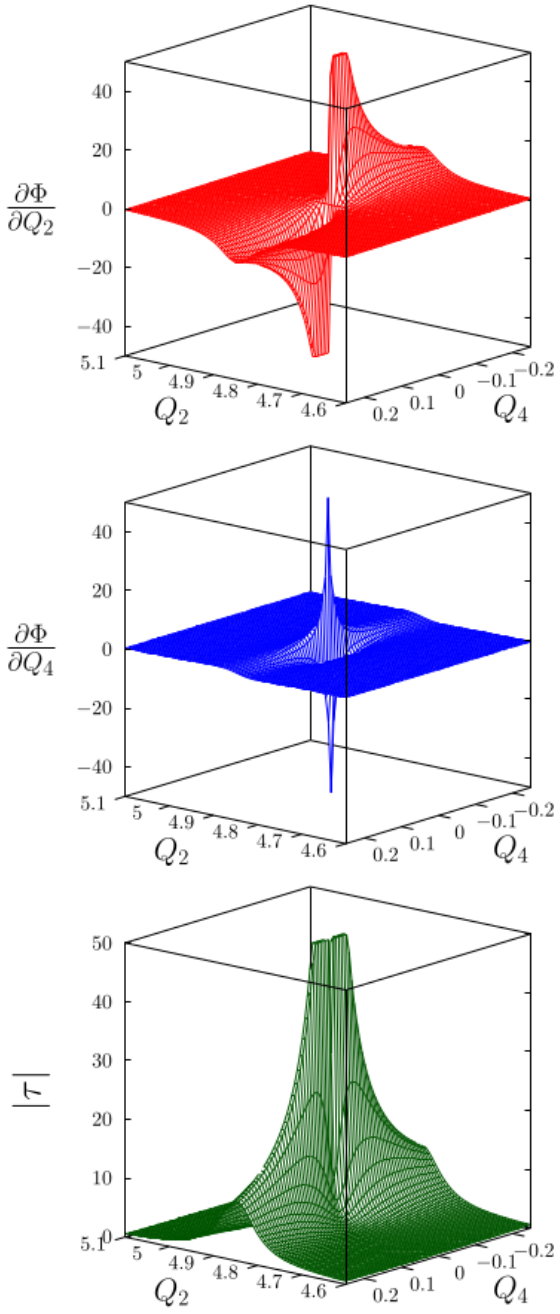

(a)

Figure 3.3: Panel (a) shows the non-adiabatic coupling terms (τ_{23Q_2} and τ_{23Q_4}) between polaritonic surfaces of H_2CO with respect to the Q_2 and Q_4 coordinates, respectively. Panel (b) shows the absolute values of these coupling terms ($|\tau_{23}| = \sqrt{\tau^2_{23Q_2} + \tau^2_{23Q_2}}$). The same cavity parameters are employed: $\omega_c = 29\ 000$ cm^{-1} au and $g = 5.34 \times 10^{-2}$.

3.2.2 The presence of the geometric phase

In this subsection, we will continue our research to study the topological properties of the H_2CO molecule by calculating the Berry phase. As discussed earlier, the total molecular wave function must possess a single value. We introduce the geometric phase (GP) factor into the adiabatic wave functions to provide the single-valued nature of the total wave function.

The Berry (or geometric) phase can be calculated by using the line integral technique [4, 7, 21], in which the value of the line integral of the NACT over a contour Γ_{con} within the configuration space equals the ADT angle (γ), which can be calculated according to the form:

$$\gamma_{23}(\Gamma_{con}) = \int_{\Gamma_{con}} \tau_{23}(s') \cdot ds', \tag{3.2.2}$$

where τ_{23} is the NAC term between the lower and upper polaritonic PESs (eq. 3.2.1). The Berry phase α_{23} can be obtained if the contour Γ_{con} is closed,

$$\alpha_{23} = \oint_{\Gamma_{con}} \tau_{23}(s') \cdot ds'. \tag{3.2.3}$$

The corresponding adiabatic states alter their signs while being transported continuously along a closed contour near the point of conical intersection. As a result of the sign change of the adiabatic states, it can be confirmed that the form (in eq. 3.2.4) can also determine the value of the Berry phase:

$$\alpha_{23} = \pi \times \begin{cases} 2n+1, & \text{if } \Gamma \text{ encircles an odd number of CIs} \\ 2n, & \text{if } \Gamma \text{ encircles an even number of CIs} \end{cases} \tag{3.2.4}$$

where the $n = 0, \pm1, \pm2, \pm3, ...$ It is much easier to determine the number of CIs in the system by checking the value of α_{23} related to the ADT angle $\gamma_{23}(\Gamma_{con})$ (see eq. 3.2.2).

In Figure 3.4, the geometric arrangement of the two various paths ap-

plied in the geometric phase calculations is demonstrated with three distinct coupling strengths ($g = 5.34 \times 10^{-3}$ au, $g = 5.34 \times 10^{-2}$ au, $g = 5.34 \times 10^{-1}$ au) and a frequency ($\omega_c = 29\ 000\ \mathrm{cm}^{-1}$). In the top panel, the two distinct paths, P_0 and P_1, are shown near the LICI. Only one of them, P_1, encompasses the point of the light-induced conical intersection. In the middle panel, the transformation angle's values for these two distinct counters are demonstrated. It is clear that the Berry phase values for the two closed paths equal 0 and $-\pi$, respectively, regardless of the applied three different cavity coupling strengths (see the middle panel in Fig. 3.4). These obtained values of α_{23} fully corroborate the statements of equations 3.2.3 and 3.2.4. The NACT's line integral value must equal zero whenever the value of the ADT angle does not alter near the closed circle. Therefore, a zero value of α_{23} means that any LICI is not found in the case of the P_0, while the value of α_{23} corresponds to the odd number of the CIs (that is, one LICI) for the case of the P_1 closed path.

In order to gain deeper insight into the numerical findings, a three-dimensional figure reveals the ADT transformation angle over the branching space (Q_2, Q_4) in the bottom panel of Figure 3.4. The cavity parameters have been chosen as $g = 5.34 \times 10^{-2}$ au and $\omega_c = 29\ 000\ \mathrm{cm}^{-1}$. It can be seen that the curve corresponding to the P_0 closed path does not have any shift along the one-circle path of Φ. In contrast, a shift along the one-circle path of Φ equals π for the case of the P_1 closed path encircling the point of LICI. The shift is closely associated with the Berry phase calculated from the line integral of the non-adiabatic coupling terms. In addition to the line integral technique (eq. 3.2.3), it is possible to evaluate the Berry phase by obtaining the difference of Φ for a closed path as follows:

$$\alpha_{23} = \Phi(s_0)_{\text{end of the path}} - \Phi(s_0)_{\text{beginning of the path}}. \tag{3.2.5}$$

The results from the bottom panel of Figure 3.4 fully verify the statement of eq. 3.2.5.

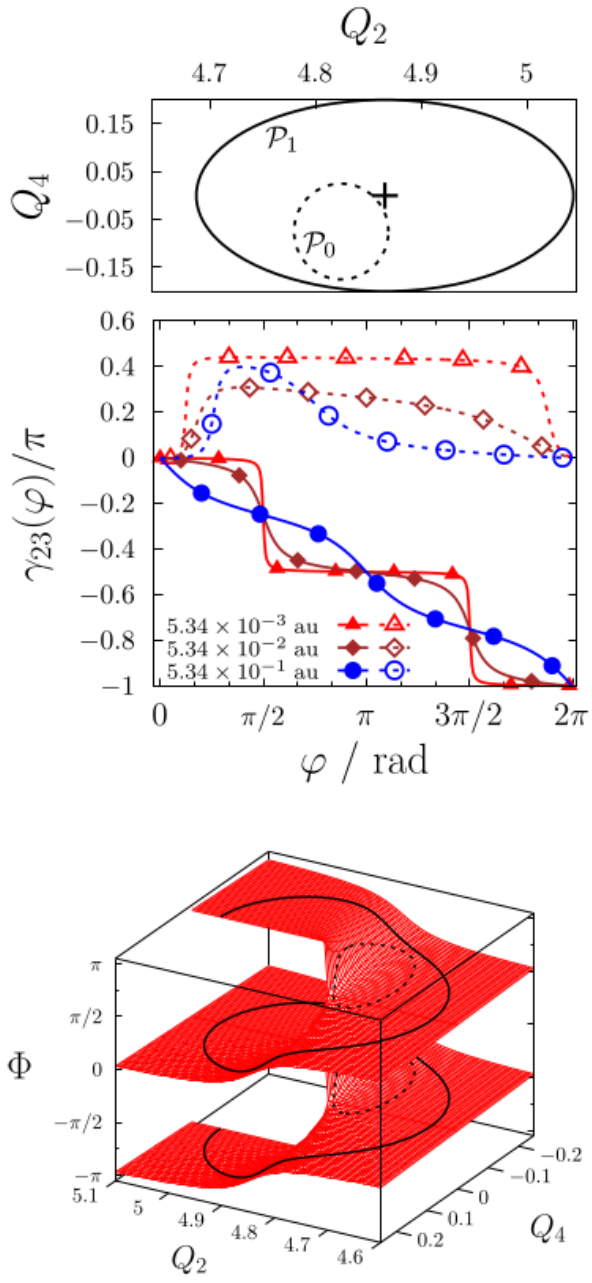

Figure 3.4: Geometric configuration of the two various paths utilized in geometric phase calculations is depicted. These two distinct paths, P_0 and P_1, are illustrated. Only the P_1 closed path encompasses the cavity-induced conical intersection (top panel). In the middle panel, the line integral of the non-adiabatic couplings (NACs) with respect to position along the two studied circles are presented. The curves marked with filled markers correspond to calculations along a contour surrounding the LICI. A single cavity frequency (ω_c = 29 000 cm^{-1}) with three various coupling strengths ($g = 5.34 \times 10^{-3}$ au, $g = 5.34 \times 10^{-2}$ au, $g = 5.34 \times 10^{-1}$ au) is utilized. In the bottom panel, a three-dimensional figure that illustrates the transformation angle as functions of Q_2 and Q_4 is displayed, where the applied frequency and coupling strength of the cavity equal ω_c = 29 000 cm^{-1} and $g = 5.34 \times 10^{-2}$ au, respectively.

3.3 Conclusion

The light-induced topological features of the H_2CO molecule are studied in the confined optical cavity. The non-adiabatic coupling terms between two polaritonic states and their absolute values are calculated in the vicinity of the LICI created by the cavity. The numerical results obtained for the NAC terms and their absolute values clearly show the fingerprint of cavity-induced non-adiabatic properties near the LICI.

The Berry phase is calculated using the line integral technique around the LICI. The Berry phase calculations are equal to $\alpha_{23} = \pi$ for the closed path encompassing the LICI and $\alpha_{23} = 0$ for the closed path not encompassing the LICI. As known from the natural conical intersection theory, these results can provide clear evidence of the existence of LICI in the system.

Chapter 4

Summary

In this thesis, I present the results of investigations into the light-induced non-adiabatic molecular properties of diatomic and polyatomic molecular systems under external fields.

Any numerical calculations of the nuclear dynamics of molecules may not be done without the proper explanation of the molecular electronic structure data. These relevant data are the potential energy surfaces and dipole moments (PDMs, TDMs). These electronic structure computations were always needed to study the nuclear dynamics of the system using the time-dependent Schrödinger equation. To study time-dependent molecular dynamics, I utilized today's modern numerical package, MCTDH, developed by the Heidelberg group.

One of my works focused on laser-induced molecular dissociation dynamics in the presence of two LICIs and one LIAC created by the pump and probe pulses and the impact of the system's PDMs on the dissociation. My second project investigated the topological aspects of cavity-induced degeneracies in H_2CO.

Electronic structure calculations

I carried out ab initio calculations of electronic orbitals to obtain the PDMs, TDMs and PESs for the NaH system (chapter 2) using the MRCI method at

the high-level basis set in the MOLPRO package. In the calculations, only two electrons out of twelve are active in two molecular orbitals (in the A_1 irreducible representation). In contrast, the remaining electrons are fully occupied in the A_1, B_1 and B_2 irreducible representations. This electron structure of this molecule gives us reasonable data that agrees with others in the literature.

For the H_2CO molecule (chapter 3), the electronic structure calculations have been calculated to get the PDMs, TDMs, and PESs at the CAM-B3LYP/6-31G* level of theory. These data are interpolated using the GSL package in the high-level spline type.

Molecular dissociation dynamics in NaH

In the pump-probe scheme, I investigated the molecular dissociation dynamics of NaH involving the three lowest electronic states and the influence of the system's rotational motion on the dissociation. When the pump and probe pulses are applied to the system, two LICIs are formed between the two excited states and a LIAC between the ground and the first excited states. Two LICIs between the two excited states and a LIAC between the ground and the first excited states are formed when the pump and probe pulses are applied to the system. In the presence of these LICIs and LIAC, I investigated the dissociation probabilities of the individual electronic states of this system as a function of delay time.

The results show that dissociation occurs mainly in the second excited electronic state due to the dissociative state and the pulses used. Similarly, the dissociation happens in the ground electronic state due to the probe effect. However, a rich pattern of the dissociation probability on the $V_A(R)$ state has been observed. This complexity of the dissociation is partially explained by several factors, like the two-photon effect, transferring the population back to the $V_B(R)$ state from the $V_A(R)$ state. I also did some additional calculations by artificially changing the values of the PDMs, even TDMs, so as to explain the spike-like peaks on the dissociation of $V_A(R)$.

To fully explain the properties of the dissociation on the $V_A(R)$ state, some additional simulations need to be performed by changing the parameters of the pump and the probe; this will be our next project.

To further analyze the system's dissociation dynamics, I carried out numerical simulations of the fragment KER and angular distributions of the individual electronic states as a function of delay time. These calculations are performed for the short and long delay periods in 1D and 2D. The results have shown that the effects of the molecular rotation, LICIs/LIAC, and the different magnitudes/directions of the TDMs led to discrepancies in results between the 1D and 2D calculations.

The impact of the PDM on the dissociation dynamics in NaH

To study the influence of the PDM of the NaH system on the dissociation dynamics, I performed additional calculations in the 1D and 2D frameworks with and without PDMs. The attained data has clearly shown that this molecule's permanent dipole moment played a minor role in the total dissociation probability, at least for the applied laser parameters. The impact of PDM on the dissociation yields of the $V_X(R)$ and $V_B(R)$ states is practically negligible. Conversely, the PDM significantly influences the dissociation of $V_A(R)$. When the system's PDM is included in the calculations, pronounced peak-like patterns appear in the dissociation yield on $V_A(R)$.

Topological features

Chapter 3 was dedicated to studying the topological features of the polyatomic formaldehyde (H_2CO) molecule in an optical cavity. This system has no natural conical intersection around the FC region and any first-order non-adiabatic coupling between the ground and first excited electronic states near its equilibrium arrangement. Therefore, with the help of

the single cavity mode, two polaritonic or adiabatic electronic states and the resulting LICI between these polaritonic states are created to investigate the topological aspects of this system. The diagonalization method is used to obtain the polaritonic electronic states in numerical calculations. All computational calculations are conducted in the two-dimensional model (ν_2, ν_4), where the vibrational mode ν_2 is considered as the tuning mode, while the mode ν_4 is considered as the coupling mode.

The line integral technique is used to compute the geometric (or Berry) phase near LICI. The obtained results have shown that the Berry phase equals π for the closed path encompassing the LICI and 0 for the closed path not encompassing the LICI. As known from the theory of the natural conical intersection, only the closed path, which encompasses the LICI, discovered one LICI (already created by the cavity quantum light) in the system.

The non-adiabatic coupling terms between the two polaritonic states and the absolute values of the NACTs around LICI are computed. The results obtained from the NAC terms clearly show the fingerprint of light-induced non-adiabatic phenomena.

Acknowledgments

First of all, I am very grateful to my supervisor, Dr. Ágnes Vibók, for the valuable discussions, the encouragements and all her instructions in the scientific field. Her support and guidelines always motivated my PhD studies forward, and she always provided me with proper working conditions.

I would like to express my many thanks to Dr. Gábor Halász, who helped me learn theoretical computational physics. I'm thankful to him for finding the time to answer my many questions. I have been learning a lot from him, not only computational knowledge but also physics.

I would like to acknowledge Dr. Csehi András, who introduced me to electronic structure calculations. I sincerely appreciate his willingness to share his knowledge and skills with MOLPRO, which has greatly enriched my understanding of this field.

I would like to thank Dr. Péter Badankó for sharing his experience and knowledge in the field of MCTDH.

Last but not least, I am thankful to my dear Mother and Father and my own Family for supporting me throughout the years.

Finally, I would like to express my gratitude for the financial assistance provided by the following sources: This work would not have been done without the Stipendium Hungaricum Scholarship established by the Hungarian Government. Many thanks for the sources provided by the EU-funded Hungarian grant EFOP.

Publication list

The Thesis is based on the following publications.

P1. Otabek Umarov, András Csehi, Péter Badankó, Gábor J. Halász, and Ágnes Vibók. Light-induced photodissociation on the lowest three electronic states of NaH molecule. *Physical Chemistry Chemical Physics*, 26,7211, 2024.

P2. Péter Badankó, Otabek Umarov, Csaba Fábri, Gábor J. Halász, and Ágnes Vibók. Topological aspects of cavity-induced degeneracies in polyatomic molecules. *International Journal of Quantum Chemistry*, 122(8):e26750, 2022.

The publications that are NOT included in the Thesis.

P3. Dilfuza Umarova, Otabek Umarov, Attila Tóth and András Csehi. Spectral evidence of vibronic Rabi oscillations in the resonance-enhanced photodissociation of MgH^+. *Physical Review A*, 2024.

Talks

1. O. Umarov: Topological aspects of light-induced degeneracies in polyatomic molecules, "TSRC - Quantum Frontiers in Molecular Science", $6^{th} - 10^{st}$ June 2022, Telluride, USA

2. O. Umarov: Topological aspects of light-induced degeneracies in polyatomic molecules, international scientific conference, 20^{st} May 2023, Jizzakh polytechnical institute, Uzbekistan

3. O. Umarov: Light-induced photodissociation dynamics in NaH, Seminar, 3^{rd} May 2024, Department of Optics and Spectroscopy, Samarkand State University, Uzbekistan

Posters

1. P. Badankó, O. Umarov, C. Fábri, T. Szidarovszky, Á. Vibók, G. J. Halász: Topological aspects of quantum light-induced conical intersections, "Local vs Collective Interactions in Polaritonic Chemistry, CECAM-FR-GSO", $22^{nd} - 24^{st}$ June 2022, University of Bordeaux, France.

2. P. Badankó, O. Umarov, C. Fábri, T. Szidarovszky, Á. Vibók, G. J. Halász: Topological aspects of quantum light-induced conical intersections, "ECAMP14, 14^{th} European Conference on Atoms Molecules and Photons", June 27 - July 1, 2022, Vilnius, Lithuania.

3. O. Umarov, A. Csehi, P. Badankó, G. J. Halász and Á. Vibók: Light-induced photodissociation on the lowest three electronic states of NaH molecule, Attochem conference, February 28 - March 1, 2024, University of La Laguna, Tenerife, Canary Islands (Spain)

References

[1] Max Born and W Heisenberg. Zur quantentheorie der molekeln. *Original Scientific Papers Wissenschaftliche Originalarbeiten*, pages 216–246, 1985.

[2] John Von Neumann and Eugene Wigner. No crossing rule. *Z. Phys*, 30:467–470, 1929.

[3] H Köuppel, Wolfgang Domcke, and Lorenz S Cederbaum. Multimode molecular dynamics beyond the born-oppenheimer approximation. *Advances in chemical physics*, pages 59–246, 1984.

[4] Michael Baer. *Beyond Born-Oppenheimer: electronic nonadiabatic coupling terms and conical intersections*. John Wiley & Sons, 2006.

[5] Graham A Worth and Lorenz S Cederbaum. Beyond born-oppenheimer: Molecular dynamics through a conical intersection. *Annu. Rev. Phys. Chem.*, 55:127–158, 2004.

[6] Csaba Fábri, Gábor J Halász, Lorenz S Cederbaum, and Ágnes Vibók. Born–oppenheimer approximation in optical cavities: from success to breakdown. *Chemical Science*, 12(4):1251–1258, 2021.

[7] Michael Baer. Introduction to the theory of electronic non-adiabatic coupling terms in molecular systems. *Physics Reports*, 358(2):75–142, 2002.

[8] Péter Badankó, Otabek Umarov, Csaba Fabri, Gabor J Halasz, and Ágnes Vibók. Topological aspects of cavity-induced degeneracies in polyatomic molecules. *International Journal of Quantum Chemistry*, 122(8):e26750, 2022.

[9] Wolfgang Domcke, David R Yarkony, and Horst Köppel. *Conical intersections: theory, computation and experiment*, volume 17. World Scientific, 2011.

[10] András Csehi, Gábor J Halász, Lorenz S Cederbaum, and Ágnes Vibók. Intrinsic and light-induced nonadiabatic phenomena in the nai molecule. *Physical Chemistry Chemical Physics*, 19(30):19656–19664, 2017.

[11] Tamás Szidarovszky, Gábor J Halász, and Ágnes Vibók. Three-player polaritons: nonadiabatic fingerprints in an entangled atom–molecule–photon system. *New Journal of Physics*, 22(5):053001, 2020.

[12] András Csehi, Ágnes Vibók, Gábor J Halász, and Markus Kowalewski. Quantum control with quantum light of molecular nonadiabaticity. *Physical Review A*, 100(5):053421, 2019.

[13] Tamás Szidarovszky, Péter Badankó, Gábor J Halász, and Ágnes Vibók. Nonadiabatic phenomena in molecular vibrational polaritons. *The Journal of Chemical Physics*, 154(6), 2021.

[14] Lorenz S Cederbaum, Ying-Chih Chiang, Philipp V Demekhin, and Nimrod Moiseyev. Resonant auger decay of molecules in intense x-ray laser fields: light-induced strong nonadiabatic effects. *Physical Review Letters*, 106(12):123001, 2011.

[15] Csaba Fábri, Benjamin Lasorne, Gábor J Halász, Lorenz S Cederbaum, and Ágnes Vibók. Quantum light-induced nonadiabatic phenomena in the absorption spectrum of formaldehyde: Full-and reduced-

dimensionality studies. *The Journal of Chemical Physics*, 153(23), 2020.

[16] Csaba Fábri, Gábor J Halász, Lorenz S Cederbaum, and Ágnes Vibók. Signatures of light-induced nonadiabaticity in the field-dressed vibronic spectrum of formaldehyde. *The Journal of Chemical Physics*, 154(12), 2021.

[17] András Csehi, Gábor J Halász, Lorenz S Cederbaum, and Ágnes Vibók. Competition between light-induced and intrinsic nonadiabatic phenomena in diatomics. *The Journal of Physical Chemistry Letters*, 8(7):1624–1630, 2017.

[18] Csaba Fábri, Benjamin Lasorne, Gábor J Halász, Lorenz S Cederbaum, and Ágnes Vibók. Striking generic impact of light-induced non-adiabaticity in polyatomic molecules. *The Journal of Physical Chemistry Letters*, 11(13):5324–5329, 2020.

[19] Wolfgang Domcke, David Yarkony, and Horst Köppel. *Conical intersections: electronic structure, dynamics & spectroscopy*, volume 15. World Scientific, 2004.

[20] Philipp V Demekhin and Lorenz S Cederbaum. Light-induced conical intersections in polyatomic molecules: General theory, strategies of exploitation, and application. *The Journal of chemical physics*, 139(15), 2013.

[21] Gábor J Halász, Ágnes Vibók, Milan Šindelka, Nimrod Moiseyev, and Lorenz S Cederbaum. Conical intersections induced by light: Berry phase and wavepacket dynamics. *Journal of Physics B: Atomic, Molecular and Optical Physics*, 44(17):175102, 2011.

[22] Spiridoula Matsika. Conical intersections in molecular systems. *Reviews in computational chemistry*, 23:83, 2007.

[23] Michael Baer. Adiabatic and diabatic representations for atom-molecule collisions: Treatment of the collinear arrangement. *Chemical Physics Letters*, 35(1):112–118, 1975.

[24] Nimrod Moiseyev, Milan Šindelka, and Lorenz S Cederbaum. Laser-induced conical intersections in molecular optical lattices. *Journal of Physics B: Atomic, Molecular and Optical Physics*, 41(22):221001, 2008.

[25] Milan Šindelka, Nimrod Moiseyev, and Lorenz S Cederbaum. Strong impact of light-induced conical intersections on the spectrum of diatomic molecules. *Journal of Physics B: Atomic, Molecular and Optical Physics*, 44(4):045603, 2011.

[26] Gábor J Halász, Agnes Vibók, Nimrod Moiseyev, and Lorenz S Cederbaum. Light-induced conical intersections for short and long laser pulses: Floquet and rotating wave approximations versus numerical exact results. *Journal of Physics B: Atomic, Molecular and Optical Physics*, 45(13):135101, 2012.

[27] Gábor J Halász, Á Vibók, and Lorenz S Cederbaum. Direct signature of light-induced conical intersections in diatomics. *The Journal of Physical Chemistry Letters*, 6(3):348–354, 2015.

[28] Wendell T Hill III and Chi H Lee. *Light-Matter interaction: Atoms and molecules in external fields and nonlinear optics*, volume 2. John Wiley & Sons, 2006.

[29] Mitchel Weissbluth. *Atoms and molecules*. Elsevier, 2012.

[30] James A Hutchison, Tal Schwartz, Cyriaque Genet, Eloïse Devaux, and Thomas W Ebbesen. Modifying chemical landscapes by coupling to vacuum fields. *Angewandte Chemie International Edition*, 51(7):1592–1596, 2012.

[31] Javier Galego, Francisco J Garcia-Vidal, and Johannes Feist. Cavity-induced modifications of molecular structure in the strong-coupling regime. *Physical Review X*, 5(4):041022, 2015.

[32] András Csehi, Markus Kowalewski, Gábor J Halász, and Ágnes Vibók. Ultrafast dynamics in the vicinity of quantum light-induced conical intersections. *New Journal of Physics*, 21(9):093040, 2019.

[33] Basile FE Curchod and Federica Agostini. On the dynamics through a conical intersection. *The journal of physical chemistry letters*, 8(4):831–837, 2017.

[34] Changjian Xie, Bin Zhao, Christopher L Malbon, David R Yarkony, Daiqian Xie, and Hua Guo. Insights into the mechanism of nonadiabatic photodissociation from product vibrational distributions. the remarkable case of phenol. *The Journal of Physical Chemistry Letters*, 11(1):191–198, 2019.

[35] KR Shamasundar, Gerald Knizia, and Hans-Joachim Werner. A new internally contracted multi-reference configuration interaction method. *The Journal of Chemical Physics*, 135(5), 2011.

[36] Hans-Joachim Werner, Peter J Knowles, Gerald Knizia, Frederick R Manby, and Martin Schütz. Molpro: a general-purpose quantum chemistry program package. *Wiley Interdisciplinary Reviews: Computational Molecular Science*, 2(2):242–253, 2012.

[37] Michael H Beck, Andreas Jäckle, Graham A Worth, and H-D Meyer. The multiconfiguration time-dependent hartree (mctdh) method: a highly efficient algorithm for propagating wavepackets. *Physics reports*, 324(1):1–105, 2000.

[38] Hans-Dieter Meyer, Fabien Gatti, and Graham A Worth. *Multidimensional quantum dynamics: MCTDH theory and applications*. John Wiley & Sons, 2009.

[39] Hans-Dieter Meyer. Studying molecular quantum dynamics with the multiconfiguration time-dependent hartree method. *Wiley Interdisciplinary Reviews: Computational Molecular Science*, 2(2):351–374, 2012.

[40] GA Worth, MH Beck, A Jäckle, H-D Meyer, F Otto, M Brill, and O Vendrell. The heidelberg mctdh package: A set of programs for multi-dimensional quantum dynamics. 2023.

[41] Jerzy Leszczynski. *Handbook of computational chemistry*, volume 3. Springer Science & Business Media, 2012.

[42] Attila Szabo and Neil S Ostlund. *Modern quantum chemistry: introduction to advanced electronic structure theory*. Courier Corporation, 2012.

[43] Trygve Helgaker, Poul Jorgensen, and Jeppe Olsen. *Molecular electronic-structure theory*. John Wiley & Sons, 2013.

[44] Marcos Dantus and Ahmed Zewail. Introduction: femtochemistry, 2004.

[45] Brian Harold Bransden and Charles Jean Joachain. *Physics of atoms and molecules*. Pearson Education India, 2003.

[46] Claude Cohen-Tannoudji, Jacques Dupont-Roc, and Gilbert Grynberg. *Atom-photon interactions: basic processes and applications*. John Wiley & Sons, 1998.

[47] Csaba Fábri, András Csehi, Gábor J Halász, Lorenz S Cederbaum, and Ágnes Vibók. Classical and quantum light-induced non-adiabaticity in molecular systems. *AVS Quantum Science*, 6(2), 2024.

[48] Arkajit Mandal, Sebastian Montillo Vega, and Pengfei Huo. Polarized fock states and the dynamical casimir effect in molecular cavity

quantum electrodynamics. *The Journal of Physical Chemistry Letters*, 11(21):9215–9223, 2020.

[49] Hans-Dieter Meyer. Introduction to mctdh. 2011.

[50] A Jäckle and H-D Meyer. Reactive scattering using the multiconfiguration time-dependent hartree approximation: General aspects and application to the collinear h+ h2→ h2+ h reaction. *The Journal of chemical physics*, 102(14):5605–5615, 1995.

[51] Uwe Manthe, H-D Meyer, and LS Cederbaum. Multiconfigurational time-dependent hartree study of complex dynamics: Photodissociation of no2. *The Journal of chemical physics*, 97(12):9062–9071, 1992.

[52] Jian-Yun Fang and Hua Guo. Multiconfiguration time-dependent hartree studies of the ch3i/mgo photodissociation dynamics. *The Journal of chemical physics*, 101(7):5831–5840, 1994.

[53] UV Riss and H-D Meyer. Investigation on the reflection and transmission properties of complex absorbing potentials. *The Journal of chemical physics*, 105(4):1409–1419, 1996.

[54] Daniel Peláez and Hans-Dieter Meyer. On the infrared absorption spectrum of the hydrated hydroxide (h3o2-) cluster anion. *Chemical Physics*, 482:100–105, 2017.

[55] Qingyong Meng and Hans-Dieter Meyer. A full-dimensional multilayer multiconfiguration time-dependent hartree study on the ultraviolet absorption spectrum of formaldehyde oxide. *The Journal of Chemical Physics*, 141(12), 2014.

[56] Eric E Aubanel and Andre D Bandrauk. Rapid vibrational inversion via time gating of laser-induced avoided crossings in high-intensity photodissociation. *The Journal of Physical Chemistry*, 97(48):12620–12624, 1993.

[57] Attila Tóth, András Csehi, Gábor J Halász, and Ágnes Vibók. Photodissociation dynamics of the lif molecule: Two-and three-state descriptions. *Physical Review A*, 99(4):043424, 2019.

[58] Mohamad Saab, Matthieu Sala, Benjamin Lasorne, Fabien Gatti, and Stéphane Guérin. Full-dimensional control of the radiationless decay in pyrazine using the dynamic stark effect. *The Journal of Chemical Physics*, 141(13), 2014.

[59] Jesús González-Vázquez, Ignacio R Sola, Jesus Santamaria, and Vladimir S Malinovsky. Quantum control of spin–orbit coupling by dynamic stark-shifts induced by laser fields. *Chemical physics letters*, 431(4-6):231–235, 2006.

[60] Sebastián Carrasco, José Rogan, Juan Alejandro Valdivia, Bo Y Chang, Vladimir S Malinovsky, and Ignacio R Sola. Circularly polarized light-induced potentials and the demise of excited states. *Physical Chemistry Chemical Physics*, 24(5):2966–2973, 2022.

[61] Fabien Gatti. Molecular dynamics simulated by photons, 2018.

[62] Otabek Umarov, András Csehi, Péter Badankó, Gábor J Halász, and Ágnes Vibók. Light-induced photodissociation in the lowest three electronic states of the nah molecule. *Physical Chemistry Chemical Physics*, 26(8):7211–7223, 2024.

[63] Gábor J Halász, Ágnes Vibók, Nimrod Moiseyev, and Lorenz S Cederbaum. Nuclear-wave-packet quantum interference in the intense laser dissociation of the d 2+ molecule. *Physical Review A*, 88(4):043413, 2013.

[64] András Csehi, Gábor J Halász, Lorenz S Cederbaum, and Ágnes Vibók. Towards controlling the dissociation probability by light-induced conical intersections. *Faraday Discussions*, 194:479–493, 2016.

[65] András Csehi, Gábor J Halász, Lorenz S Cederbaum, and Ágnes Vibók. Photodissociation of d2+ induced by linearly chirped laser pulses. *The Journal of Chemical Physics*, 143(1), 2015.

[66] Tamás Szidarovszky, Gábor J Halász, Attila G Császár, Lorenz S Cederbaum, and Ágnes Vibók. Direct signatures of light-induced conical intersections on the field-dressed spectrum of na2. *The Journal of Physical Chemistry Letters*, 9(11):2739–2745, 2018.

[67] Matthias Kübel, Michael Spanner, Zack Dube, A Yu Naumov, Szczepan Chelkowski, Andrei D Bandrauk, Marc JJ Vrakking, Paul B Corkum, DM Villeneuve, and A Staudte. Probing multiphoton light-induced molecular potentials. *Nature communications*, 11(1):2596, 2020.

[68] ME Corrales, J González-Vázquez, G Balerdi, IR Solá, R De Nalda, and L Bañares. Control of ultrafast molecular photodissociation by laser-field-induced potentials. *Nature chemistry*, 6(9):785–790, 2014.

[69] Anindita Bhattacharjee and Krishna Rai Dastidar. Photodissociation of NaH. *Physical Review A*, 65(2):022701, 2002.

[70] Mireille Aymar, Johannes Deiglmayr, and Olivier Dulieu. Systematic trends in electronic properties of alkali hydrides. *Canadian Journal of Physics*, 87(5):543–556, 2009.

[71] Edward S Sachs, Juergen Hinze, and Nora H Sabelli. Transition moments, band strengths, and line strengths for NaH. *The Journal of Chemical Physics*, 62(9):3384–3388, 1975.

[72] Edward S Sachs, Juergen Hinze, and Nora H Sabelli. Mcscf calculations for six states of NaH. *The Journal of Chemical Physics*, 62(9):3367–3376, 1975.

[73] WT Zemke, RE Olson, KK Verma, WC Stwalley, and B Liu. Dipole moment and potential energy functions of the x $1\sigma+$ and a $1\sigma+$ states of NaH. *The Journal of chemical physics*, 80(1):356–364, 1984.

[74] Qianqian Guo, Jin-Wei Hu, Jianjun Qi, Jie Yu, and Yong-Chang Han. Quantum simulation of the photodissociation cross section of the NaH molecule. *Laser Physics*, 32(4):045701, 2022.

[75] Gerhard Herzberg and H Christopher Longuet-Higgins. Intersection of potential energy surfaces in polyatomic molecules. *Discussions of the Faraday Society*, 35:77–82, 1963.

[76] Hugh Christopher Longuet-Higgins. The intersection of potential energy surfaces in polyatomic molecules. *Proceedings of the Royal Society of London. A. Mathematical and Physical Sciences*, 344(1637):147–156, 1975.

[77] C Alden Mead and Donald G Truhlar. On the determination of born–oppenheimer nuclear motion wave functions including complications due to conical intersections and identical nuclei. *The Journal of Chemical Physics*, 70(5):2284–2296, 1979.

[78] Michael Victor Berry. Quantal phase factors accompanying adiabatic changes. *Proceedings of the Royal Society of London. A. Mathematical and Physical Sciences*, 392(1802):45–57, 1984.

[79] Mark Galassi, Jim Davies, James Theiler, Brian Gough, Gerard Jungman, Patrick Alken, Michael Booth, Fabrice Rossi, and Rhys Ulerich. Gnu scientific library. 2019.

[80] Jon H Shirley. Solution of the schrödinger equation with a hamiltonian periodic in time. *Physical Review*, 138(4B):B979, 1965.